

**Inelastic x-ray scattering study of plasmons
in liquid alkali metals**

Dissertation

Department of Physics, Graduate School of Science
Kyoto University

by
Koji Kimura

Abstract

The electronic states in liquid metals are less clearly understood than in the case of crystalline systems, because of the disordered structure of ions in the liquid state. Behaviors of plasmon, a collective excitation of electrons, provide useful information on how the valence electrons are influenced by the ions in liquid metals because the excitation energy and the line width of plasmon strongly reflect the electron-ion interaction.

In this study, we investigate plasmon behaviors in liquid alkali metals near the melting point. Inelastic x-ray scattering (IXS) techniques are first applied to liquid Rb and Cs, and the plasmon excitation energies (dispersion relations) and the line widths are determined as a function of the momentum transfer q . We also derive a formula for evaluating the plasmon line width in liquid metals at $q = 0$, and apply the formula to liquid alkali metals.

We find that the plasmon dispersions in liquid Rb and Cs are different from those in solid Rb and Cs. We discuss the observed difference, considering the variation in the ionic structure upon melting, and it is indicated that the effect of ions on plasmon dispersions is less important in the liquid state than in the solid state. In addition, we reveal that the line width of Rb becomes narrower upon melting near $q = 0$. This narrowing is quantitatively reproduced by our calculation using the formula for the line width at the long-wavelength limit. With the aid of this calculation, we interpret that the contribution of ionic potential to the plasmon damping reduces upon melting.

This work will provide valuable information on the relation between electronic states and the disordered ionic structure in liquid metals. Such information will be useful to study the electronic states in liquid metals not only near the melting point but also under high temperatures and high pressures. In addition, such information will lead us to clarify the electronic properties in other disordered systems, such as amorphous solids, metallic glasses, or warm dense matter.

Contents

1	Introduction	5
1.1	Fluid Metals	5
1.2	Plasmons in the Electron Gas	8
1.3	Plasmons in Solid Alkali Metals	11
1.3.1	Effect of the Ions	13
1.4	Plasmons in Liquid Metals	16
1.5	Inelastic X-ray Scattering	18
1.6	Purpose of This Study	20
2	Experimental	22
2.1	Sample Cell	22
2.1.1	Construction of Sample Cell	22
2.1.2	Sealing Test	25
2.2	Introduction of the Sample into the Cell	27
2.3	Chamber for Inelastic X-ray Scattering	29
2.4	Inelastic X-ray Scattering Beamline	32
2.5	Experimental Conditions	33
2.5.1	Measurements for Rb	33
2.5.2	Measurements for Cs	34
3	Formulation of the Plasmon Line Width in Liquid Metals	35
3.1	Derivation of the Formula	35
3.2	Application of the Formula to Alkali Metals	39

4 Plasmons in Liquid Rb	42
4.1 Results	42
4.1.1 Raw IXS Spectrum	42
4.1.2 Data Analysis	46
4.1.3 Fitting Results	49
4.2 Discussion	51
4.2.1 Excitation Energy	51
4.2.2 Line Width	55
4.3 Summary	58
5 Plasmons in Liquid Cs	59
5.1 Results	59
5.2 Discussion	64
5.3 Summary	68
6 Conclusion	69
Appendix	72

Chapter 1

Introduction

1.1 Fluid Metals

Fluid state of matter, which includes the liquid state, the gas state, and the supercritical state, covers a wide range of the phase diagram. Figure 1.1 shows the pressure-temperature phase diagram of a typical metallic element. When a liquid metal is heated at ambient pressure, the metal is transformed to a gas phase at the boiling temperature, as indicated by the dotted arrow in Fig. 1.1. On the other hand, if the pressure is applied, the vaporization is suppressed and the metal can reach the supercritical state (solid arrow in Fig. 1.1), where distinction between liquid and gas phases does not exist [1].

Along the solid arrow in Fig. 1.1, the solid metal is transformed to the liquid state (process (1)), and then the density reduces continuously from the triple point up to the supercritical region (process (2)).

In the process (1), the metallic properties are preserved in typical metals, such as alkali metals, although the long-range order of ions vanishes upon melting. The electronic properties in such liquid metals near the melting temperature are described well with the nearly free electron (NFE) model [2, 3], where the ionic potential is treated as a weak perturbation to free electrons.

While valence electrons behave as conduction electrons near the triple point, they are localized to isolated atoms or molecules in the gas phase. Therefore, in

the process (2), the electronic states should drastically change with the continuous reduction in the density. According to the experimental studies on fluid alkali metals [4, 5, 6], the electrical conductivity deviates from the NFE prediction with decreasing density, and then rapidly drops near the critical point. In addition, changes in the magnetic susceptibility [7, 8], the Knight shift [9], and the optical reflectivity [10], have been observed along the liquid-vapor coexistence curve. It has been also suggested that the variation in the electronic states is closely related to the changes in the thermodynamic [11] and structural properties [12] with increasing temperature and pressure.

Investigation of the electronic properties in fluid metals is useful to obtain more generalized understanding of electronic states in condensed matter including disordered systems, and also will provide unified descriptions of many-body systems composed of electrons and ions from the condensed liquid phase to the dilute gas phase. Thus, to clarify the dependence of the electronic properties on thermodynamic states in fluid metals is of fundamental importance.

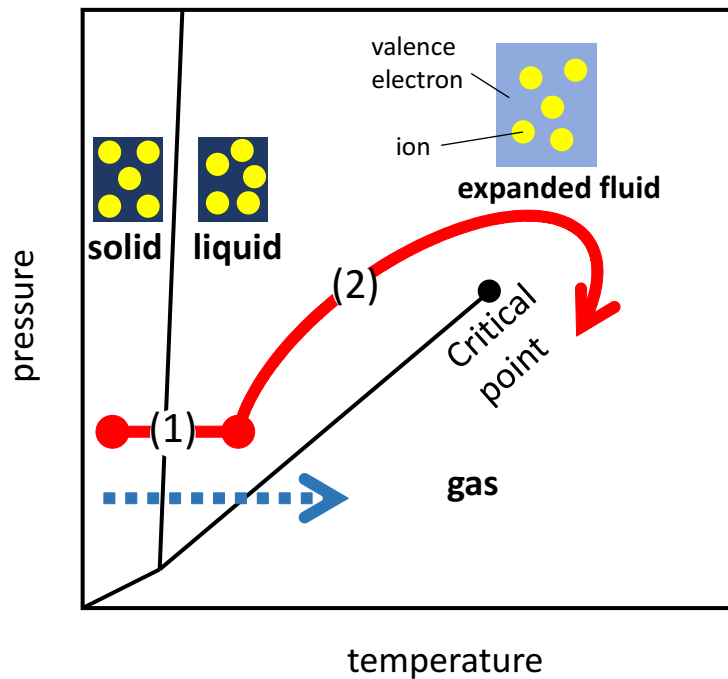


Figure 1.1: Pressure-temperature phase diagram of a typical metallic element.

Table 1.1 shows the critical temperatures (T_c) and pressures (P_c) of alkali metals [1]. The T_c and P_c of alkali metals are relatively low compared to other elements. Therefore, the temperature and pressure near critical point are accessible using laboratory techniques. Among alkali metals, the T_c and P_c of Rb and Cs are lower than lighter alkali metals, and thermodynamic conditions beyond the critical point have been achieved for these elements in various experiments [1]. In addition, alkali metals are typical simple metals, with a single valence electron which occupies a s -orbital, thus suitable to investigate intrinsic electronic properties in fluid metals.

Table 1.1: Critical temperatures (T_c) and pressures (P_c) of alkali metals. Values in italics are estimated from extrapolation of experimental data. [1]

elements	T_c ($^{\circ}\text{C}$)	P_c (bar)
Li	<i>3000</i>	<i>690</i>
Na	2210	248
K	1905	148
Rb	1744	124.5
Cs	1651	92.5

To profoundly understand the properties of fluid metals, it is required to clarify the variation in the electronic states not only in the process (2) but also in the process (1). The so-called Ziman formula [2] describes the relation between the electronic conductivity and the disordered structure in the liquid states, and well reproduces the experimental results. Jank and Hafner [13, 14] calculated electronic density of states (DOS) of liquid metals considering the disordered structure, and discussed the variations in the unoccupied DOS upon melting. These studies have provided useful information on how the electronic states are related to the ionic structure in liquid metals. However, such information has not been obtained adequately, and thus various properties in liquid metals near the melting point, such as optical properties [15] and electronic excitations [16], have been understood based on the similarity of the local structure in the liquid state to that in the solid state. Such a description does not take into account the structural disorder in liquid metals, and is inapplicable to expanded fluid systems. Considering this situation, we focus on the process (1) in this study, although our ultimate goal is to clarify the electronic

states along the liquid-vapor coexistence curve up to critical point.

In this study, we investigate plasmon behaviors in alkali metals near the melting point. As shown below, the excitation energy and the life time of the plasmon strongly reflect the electron-electron and electron-ion interactions. Therefore, investigation of plasmon behavior provides useful information to understand how the constituent particles in condensed matter interact with each other.

1.2 Plasmons in the Electron Gas

Plasmon is a quantum of the plasma oscillation, a collective excitation of electrons in plasma. This oscillation can be roughly understood as follows [17]. When there exists an excess of positive charge at some point in the plasma, electrons move to screen the positive charge and overshoot that point. They are, then, pulled back to that region, and overshoot again, and consequently the electrons start to oscillate.

The electron gas is an assembly of electrons embedded in positive uniform background. The electron gas is characterized by the r_s parameter (Wigner-Seitz radius of electrons in unit of Bohr radius) defined as

$$r_s = \left(\frac{3}{4\pi n} \right)^{1/3} a_B^{-1}, \quad (1.1)$$

where n is the electron density and a_B is the Bohr radius. Because the kinetic energy of electrons is proportional to $1/r_s^2$, and the interaction energy is proportional to $1/r_s$, the r_s parameter is proportional to the ratio of the interaction energy to the kinetic energy. Thus, the value of r_s parametrizes to what degree the interaction energy is dominant over the kinetic energy.

In the electron gas model, the excitation energy of plasmon at long-wavelength limit, ω_p , is written as

$$\omega_p = \sqrt{\frac{4\pi n e^2}{m}}, \quad (1.2)$$

where m is the electron mass, e is the elementary charge [17]. The relation between the excitation energy and the momentum transfer, that is, the plasmon dispersion

is calculated from

$$\varepsilon(q, \omega) = 0, \quad (1.3)$$

where ε is the dielectric function, q, ω are the momentum and the energy transfer, respectively [17]. For the high density region ($r_s \ll 1$), random phase approximation (RPA) [17] describes well the plasmon dispersion. In the RPA, the plasmon dispersion is given by,

$$\hbar\omega_p(q) = \hbar\omega_p + \frac{\hbar^2}{m}\alpha_{\text{RPA}}q^2 + O(q^4), \quad \alpha_{\text{RPA}} = \frac{3}{5}\frac{E_F}{\hbar\omega_p} \quad (1.4)$$

where E_F is the Fermi energy [17].

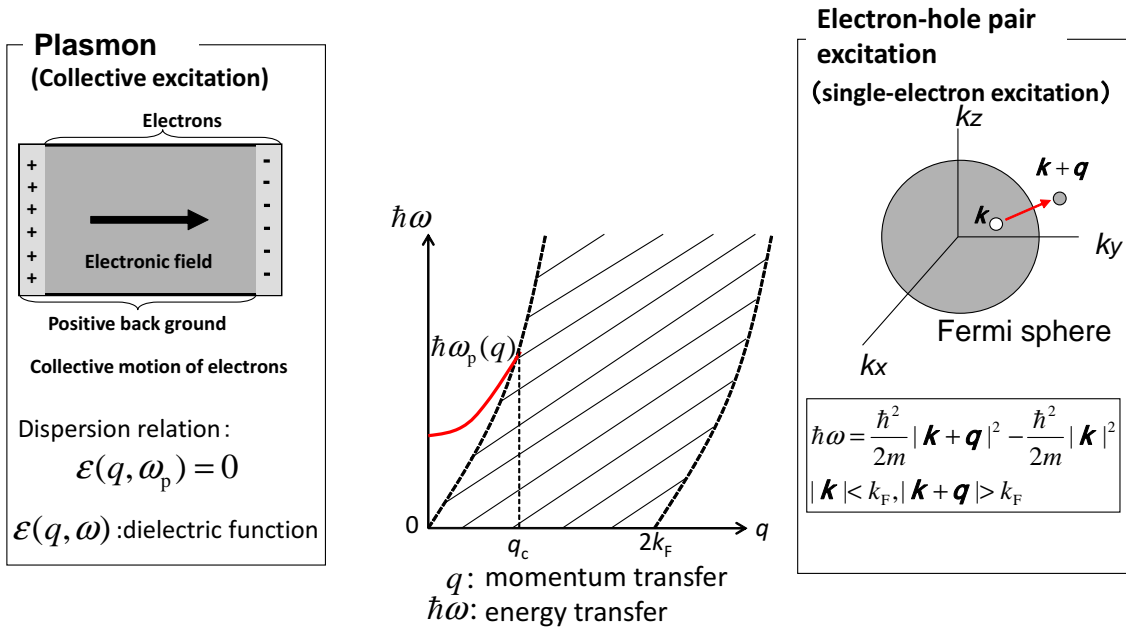


Figure 1.2: Schematic illustration of excitations in the electron gas on $(q, \hbar\omega)$ plane. Solid curve indicates the plasmon dispersion, and the shaded area shows the range on the $(q, \hbar\omega)$ plane where the electron-hole pair excitations occur.

Figure 1.2 schematically shows the excitations in the electron gas within the RPA. The plasmon dispersion relation (Eq. (1.4)) is indicated with the solid curve. The shaded area shows the range on the $(q, \hbar\omega)$ plane where the electron-hole (e-h) pair

excitations occur. This range is called e-h continuum, and determined by

$$\hbar\omega = \frac{\hbar^2}{2m}|\mathbf{k} + \mathbf{q}|^2 - \frac{\hbar^2}{2m}|\mathbf{k}|^2, \quad |\mathbf{k}| < k_F, |\mathbf{k} + \mathbf{q}| > k_F, \quad (1.5)$$

where k_F is the Fermi wave vector [17]. The plasmon dispersion curve intersects the e-h continuum at $q = q_c$. Beyond q_c , a plasmon decays into an e-h pair, and thus the life time becomes finite.

As r_s increases, the plasmon dispersion deviates from that within the RPA, because of the exchange-correlation (XC) effect. The XC effect is taken into account using the XC kernel f_{XC} , and the dispersion relation is modified as [18]

$$\hbar\omega_p(q) = \hbar\omega_p + \frac{\hbar^2}{m} \left(\alpha_{\text{RPA}} + \frac{n}{2\hbar\omega_p} f_{\text{XC}}(\omega_p) \right) q^2 + O(q^4). \quad (1.6)$$

Figure 1.3 shows the plasmon dispersion of interacting electron gas for $r_s = 2 - 10$, calculated with the quantum monte carlo method [18]. The dispersion of the plasmon becomes smaller with increasing r_s , and it becomes negative at $r_s = 10$.

In addition to the excitation energy, the life time of the plasmon is modified by the XC effect. The life time for $q > 0$ is finite even below q_c in the interacting electron gas [18, 19], while at $q = 0$ the life time is infinite.

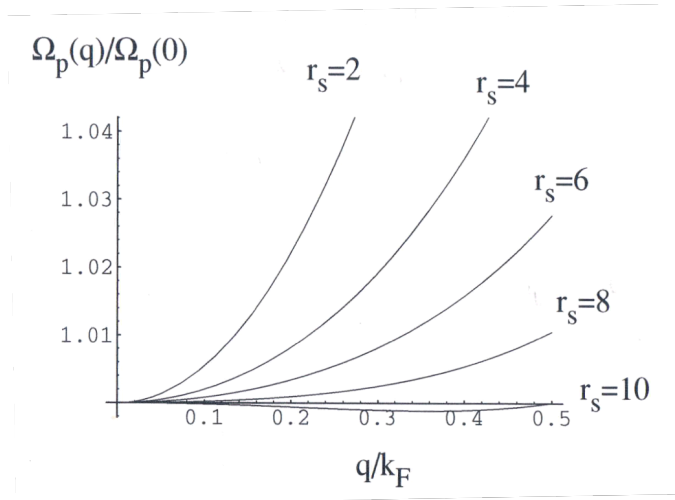


Figure 1.3: Plasmon dispersion in the interacting electron gas model, calculated with the quantum monte carlo method [18]. (reprinted from Ref. [18])

1.3 Plasmons in Solid Alkali Metals

The plasmon dispersions of solid alkali metals (Na, K, Rb, Cs) have been determined by the electron energy loss spectroscopy (EELS) experiments [20] (see Figure 1.4). The points in Fig. 1.4 are the experimental data for Na (inverted triangles, $r_s = 3.93$), K (triangles $r_s = 4.86$), Rb (circles, $r_s = 5.20$), and Cs (squares, $r_s = 5.62$). The vertical axis is normalized by the plasmon excitation energy at $q = 0$. The solid curves indicate the plasmon dispersions of the interacting electron gas model calculated by Singwi *et al.* [21] for various r_s .

As the value of r_s increases, the experimental dispersion curve shifts downwards. This behavior is qualitatively consistent with the prediction of the electron gas model. However, to reproduce the negative dispersion in Cs within the electron gas model, unrealistically large r_s value (> 10) is required. In addition, the dispersion curve of Rb shows a cusp-like shape, that is, with increasing q the plasmon energy increases up to $q/k_F \sim 0.8$, and decreases beyond $q/k_F \sim 0.8$. This behavior is not reproduced by the electron gas model.

Motivated by the EELS results for heavy alkali metals, many theoretical works have been carried out. Several researchers reconsidered the treatment of the XC effect to explain the plasmon dispersions of solid Rb and Cs [22, 23, 24, 25, 26, 27]. These studies improved the agreement with the experimental results, but the deviations from the EELS results have remained for both Rb and Cs. For Rb, the cusp-like shape has not been reproduced [22]. For Cs, although some works obtained the negative dispersion coefficient [23, 24, 25, 26], the absolute values of the dispersion coefficient were too small compared to the EELS result [23, 26], or the shape of the dispersion curve was not reproduced for the entire q range where the EELS measurements were performed [24, 25].

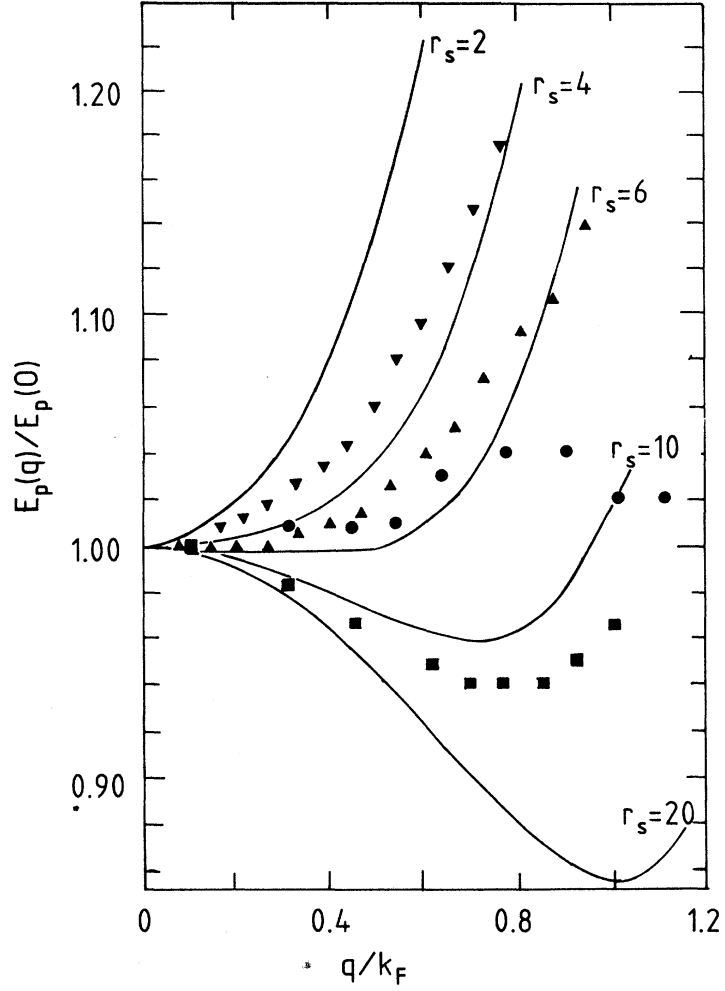


Figure 1.4: Plasmon dispersions of solid alkali metals normalized by the plasmon energy at $q = 0$, determined by the EELS measurements [20]. The symbols represent the experimental results for Na (inverted triangles), K (triangles), Rb (circles), and Cs (squares). Solid curves are the theoretical plasmon dispersions of the interacting electron gas for various r_s , calculated by Singwi *et al.* [21]. (reprinted from Ref. [20])

1.3.1 Effect of the Ions

According to the theoretical works performed by Aryasetiawan *et al.* [28], it was shown that the interband transitions to unoccupied d -states modify the plasmon energy in solid alkali metals, the so-called band structure effect. They performed the *ab initio* calculations of the plasmon dispersions in solid alkali metals (Na, K, Rb, Cs), as shown in Fig. 1.5. They showed that the band structure effect strongly lowers the plasmon energy in the heavy alkali metals, and they obtained the negative dispersion for solid Cs (Fig. 1.5). However the agreement with the experimental results is only qualitative, although their results account for the tendency that the dispersion becomes smaller as the atomic number increases from Na to Cs. In addition, the cusp-like dispersion in solid Rb was not obtained. Fleszar *et al.* [29] carried out the *ab initio* calculation of plasmon dispersion in solid Cs, considering both the XC and band structure effects. Their results agree well with the experimental results, and they attributed the negative dispersion of solid Cs to the band structure effect.

Based on the theoretical studies for the plasmon dispersions in the heavy alkali metals, both XC and band structure effects are believed to modify the plasmon dispersions in heavy alkali metals. However, the problem of the cusp-like dispersion in solid Rb has remained unsolved. Furthermore, the origin of the negative dispersion has not been clarified in a conclusive manner, because there has been no experimental study on plasmon dispersions in heavy alkali metals since the EELS experiments were performed.

Figure 1.6 shows the plasmon line width (inverse of the life time) of solid alkali metals obtained by the EELS measurements [20]. The line widths at $q = 0$ are finite in contrast to that of the electron gas model. According to the theoretical works on the plasmon line width in real metals [30, 31], the finite value of the line width at $q = 0$ originates from the interband transitions induced by the ionic potential and phonon-assisted intraband (or interband) transitions. These effects also modify the q dependence of the line width [30, 31]. Therefore, information of the electron-ion

interaction can be extracted from the plasmon line width. However, these theories can be applied only to crystalline systems, and not to disordered systems. As described below, plasmons have been observed in the disordered systems, such as liquid metals, but the plasmon line width in such systems has not been well understood.

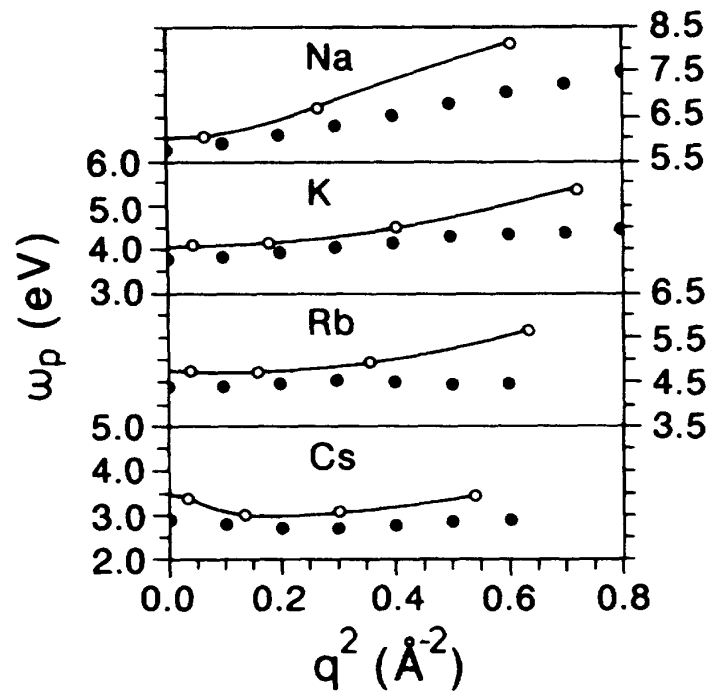


Figure 1.5: Plasmon dispersions of Na, K, Rb, and Cs. The open circles are the calculated results. The closed circles indicate the experimental results [20]. (reprinted from Ref. [28])

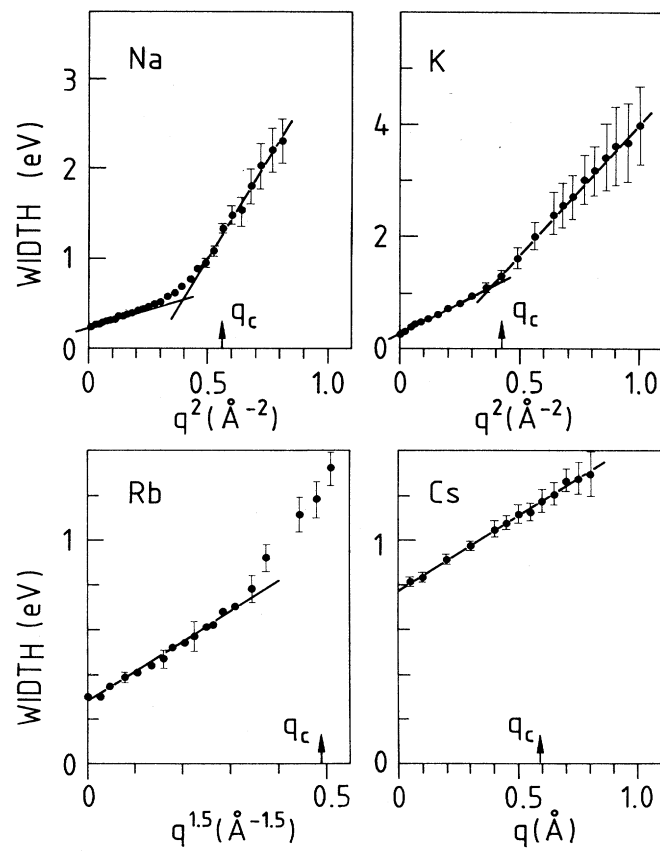


Figure 1.6: q dependence of the plasmon line width in Na, K, Rb, and Cs, obtained by the EELS experiments. (reprinted from Ref. [20])

1.4 Plasmons in Liquid Metals

Plasmons in metallic liquid have been investigated for several systems [16, 32, 33, 34, 35, 36]. Figure 1.7 (a) shows the plasmon dispersions of solid and liquid Li, obtained by the inelastic x-ray scattering (IXS) measurements. The plasmon energy becomes lower upon melting, which was explained by the reduction of the density upon melting [16]. Figure 1.7 (b) shows the q dependence of the plasmon line width of solid and liquid Li. It seems that the line width of liquid Li tends to become smaller than that of solid Li as q decreases. However the difference is small compared to the uncertainty of the data, and Hill *et al.* concluded that no change was seen in the line width upon melting. As mentioned above, interband transitions induced by the ionic potential and phonon-assisted intraband (or interband) transitions are responsible to the finite line width at $q = 0$ in the solid state [30, 31]. Hill *et al.* interpreted that the local structure of liquid Li is sufficient to mimic the crystalline structure of solid Li and the broadening of the line width was caused in the liquid state as in the case of the solid state. However, their discussion is only qualitative, and thus how the variation in the ionic structure upon melting influences the plasmon line width is not clarified.

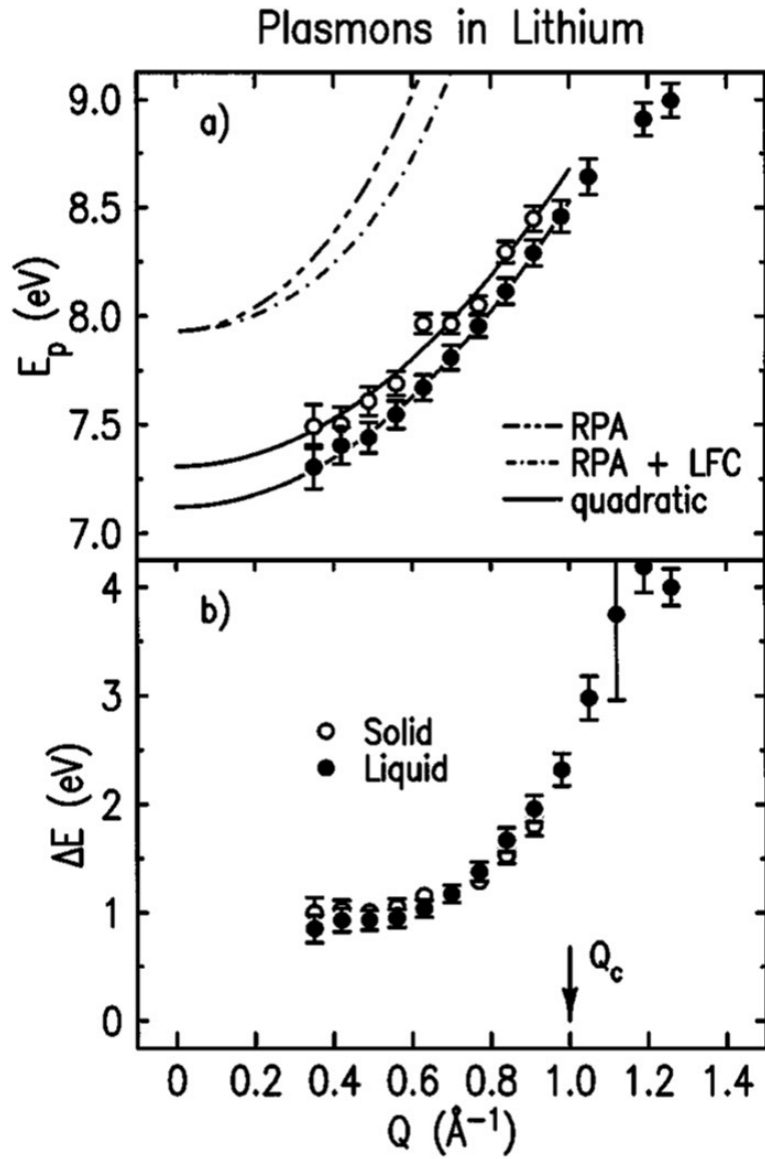


Figure 1.7: (a) Plasmon dispersions and (b) the line widths of solid (open circles) and liquid (closed circles) Li, obtained by the IXS measurements. (reprinted from Ref. [16])

1.5 Inelastic X-ray Scattering

In this study, we apply inelastic x-ray scattering (IXS) techniques to liquid alkali metals. IXS is a powerful tool to investigate electronic states in materials [37]. IXS techniques are applicable to fluid metals under various thermodynamic conditions, in contrast to electron spectroscopies such as photoelectron spectroscopy and electron energy loss spectroscopy (EELS), which require high vacuum environment.

Figure 1.8 shows the process of IXS, where the energy $\hbar\omega = \hbar\omega_2 - \hbar\omega_1$ and the momentum $\mathbf{q} = \mathbf{q}_2 - \mathbf{q}_1$ are transferred to the sample from incident x-ray. Here, $\hbar\omega_1$ ($\hbar\omega_2$) and \mathbf{q}_1 (\mathbf{q}_2) are the energy and the momentum of the incident (scattered) x-ray, respectively. If the energy transfer is much smaller than the energy of the incident x-ray ($\hbar\omega \ll \hbar\omega_1$), the momentum transfer q can be approximately represented as that of the elastic scattering,

$$q = |\mathbf{q}| = \frac{4\pi}{\lambda} \sin \theta, \quad (1.7)$$

where 2θ is the scattering angle, and λ is the wave length of the incident x-ray. In typical IXS experiments, spectra of scattered x-ray are obtained at selected scattering angles and thus scattered x-ray is measured as a function of $\hbar\omega$ and q .

Figure 1.9 shows a schematic diagram of the IXS spectrum. Depending on $\hbar\omega$, various excitations are expected to be observed, such as phonons, electron-hole pair excitations, plasmons, and core-level excitations. In this study, we focus on the energy range where plasmons and electron-hole pair excitations are observed.

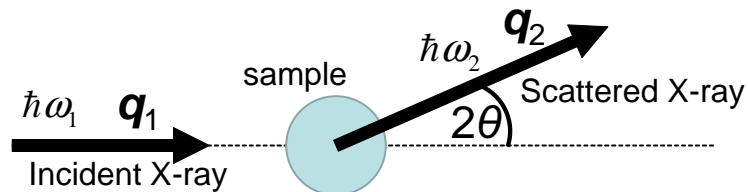


Figure 1.8: Schematic drawing of the process of inelastic x-ray scattering.

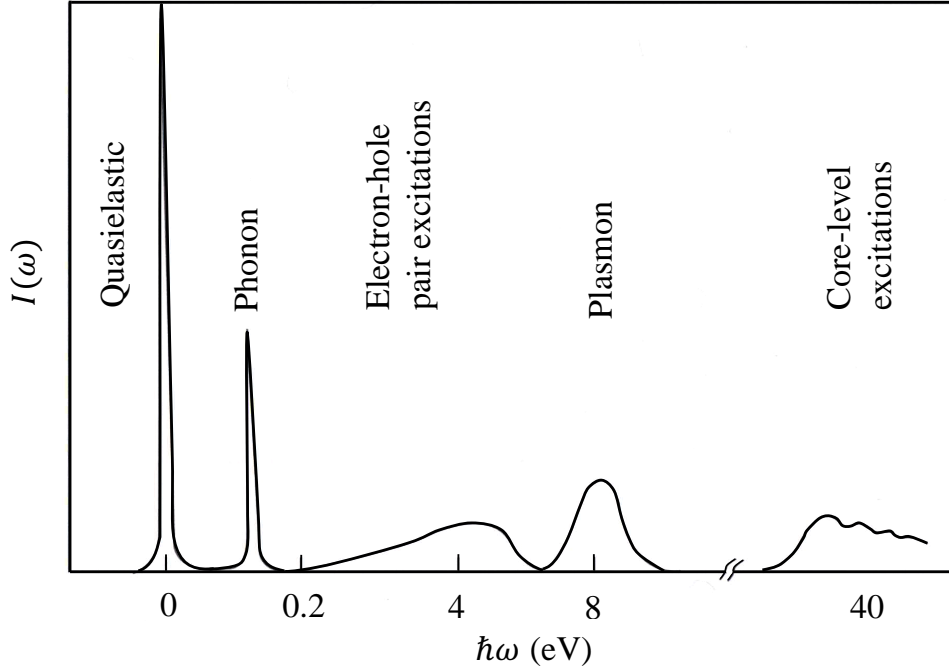


Figure 1.9: Schematic diagram of the IXS spectrum. (reprinted from ref. [37])

Plasmons can be observed also by electron energy loss spectroscopy (EELS). The cross section of EELS is much larger than IXS, and thus statistically accurate spectra are more easily obtained with EELS than with IXS. On the other hand, IXS has the following advantages over EELS. First, IXS spectra do not suffer from multiple scattering events, while influence of such events on EELS spectra increases with q , which makes it difficult to interpret the spectra. Second, IXS can be applied not only to the solid samples but also to the liquid samples [16, 32, 33, 34, 35, 36], in contrast to EELS techniques. Third, IXS is applicable even to experiments under extreme conditions such as high pressure experiments, where high pressure vessels or diamond anvil cells are used [38, 39].

Because of the smallness of the IXS cross section, early IXS experiments were performed mainly for the light elements [40, 41, 42, 43], which have small absorption coefficients. However, owing to the recent advances in synchrotron radiation sources,

the intensity and the energy resolution have been substantially improved, and IXS has become a standard tool to probe the dynamic response of electrons in materials including the heavier elements [44, 45, 46].

In this work, we study the heavy elements (Rb and Cs) in the liquid state. Therefore, synchrotron-based IXS techniques are essential for this study.

1.6 Purpose of This Study

Our ultimate goal is to clarify the plasmon behaviors in Rb and Cs along the liquid-vapor coexistence curve up to the supercritical region. However, as described in section 1.3, the plasmon behaviors in heavy alkali metals are not understood even in the solid state. Furthermore, as mentioned in section 1.4, plasmons in liquid metals have not been investigated adequately even near the melting point.

The purpose of this study is twofold. Firstly, to clarify the origin of the cusp-like dispersion in solid Rb and the negative dispersion in solid Cs. Secondly, to clarify the influence of the structural variation upon melting on the plasmon behaviors in Rb and Cs. The elucidation of the origin of the anomalous plasmon dispersions in heavy alkali metals in the solid state will give valuable information to construct more sophisticated many-body theories. In addition, this work will provide fundamental insight into the relation between electronic states and the ionic structure in disordered systems.

In this work, we perform the IXS experiments on liquid Rb and Cs near the melting point and observe plasmons. For Rb, the IXS experiments are done also in the solid state. In addition, we derive a formula to evaluate the plasmon line width of liquid metals at $q = 0$.

In the next chapter (Chapter 2), the details of the experimental method are described, such as construction of the sample cell, sample preparations, and IXS experiments at the beamline in the synchrotron radiation facility (SPring-8).

In Chapter 3, a formula for evaluating the plasmon line width of liquid metals at long-wavelength limit is derived for the first time. The formula is applied to liquid

alkali metals, and the difference of the line width in the liquid state from that in the solid state is discussed.

In Chapter 4, the results of the IXS experiments for solid and liquid Rb are presented. The variation in the plasmon dispersion upon melting, and the origin of the cusp-like dispersion in solid Rb are discussed. The difference of the line width in the liquid state from that in the solid state is also discussed, based on the formula derived in Chapter 3.

In Chapter 5, the results of the IXS experiments for liquid Cs are presented. The plasmon dispersion in the liquid state is compared with that in the solid state obtained in the previous EELS study, and difference of the dispersions between the two phases is discussed. The discussion of the negative plasmon dispersion in solid Cs is also given.

In Chapter 6, the results obtained in this work are summarized, and the significance of our study is described.

Finally, the preparation for the IXS experiments for observing plasmon in fluid alkali metals in the supercritical region is described in the appendix. Developments of a new sample cell and a high pressure vessel are described. In addition, the IXS spectra up to 1273 K at 5 MPa are presented.

Chapter 2

Experimental

2.1 Sample Cell

2.1.1 Construction of Sample Cell

In this study we measure the x-ray scattering from liquid alkali metals. Thus, we have made a sample cell to contain the liquid alkali metals [47].

Figure 2.1 shows the components of the cell. All parts are made of sapphire, which is resistant to alkali metals at moderate temperature. The cell consists of four parts, a closed-end outer pipe (inner diameter 3 mm, outer diameter 4 mm), a closed-end inner pipe (inner diameter 2.3 mm, outer diameter 3 mm), a reservoir (inner diameter 3.2 mm, outer diameter 4.5 mm), and a ring (inner diameter 4 mm, outer diameter 5 mm). Holes are drilled in the outer pipe and the ring, and a ditch is made in the outer pipe, as shown in Figs. 2.1 (a), (d). When the sample is introduced into the cell, the holes and the ditch provide a path for the liquid sample. The procedure for introducing the sample is described later.

Figure 2.2 shows the cross sectional drawing of the cell. The inner pipe is inserted into the outer pipe. The ring is put on the outer pipe, and the reservoir is joined to the ring. All parts are connected by a high-temperature ceramic adhesive (SEM-COM Co. Inc. Type SCE-1). The incident x-ray is irradiated as indicated by the arrow and the scattered x-ray goes out to the left. The closed-ends of the pipes

correspond to the x-ray windows. The space between the closed-ends of outer and inner pipes corresponds to the sample space. The thickness of the x-ray windows is made very thin (100 - 150 μm), to reduce the absorption of the x-ray by the windows.

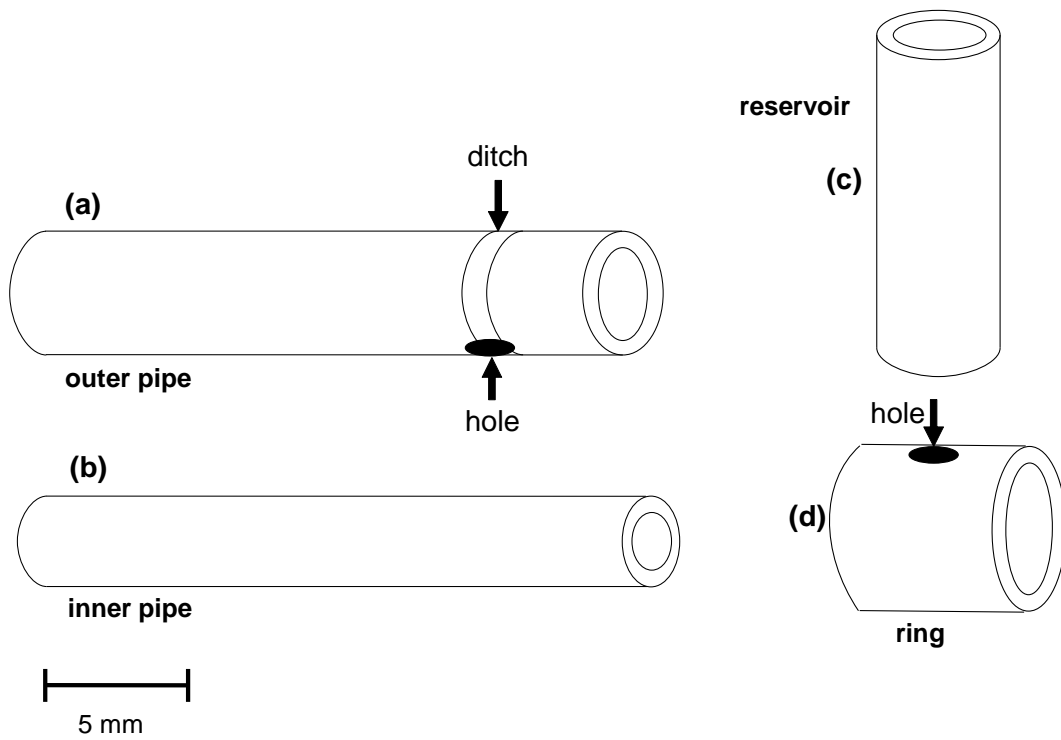


Figure 2.1: Schematic drawing of the parts of the sample cell, (a) a closed-end outer pipe, (b) a closed-end inner pipe, (c) a reservoir, and (d) a ring.

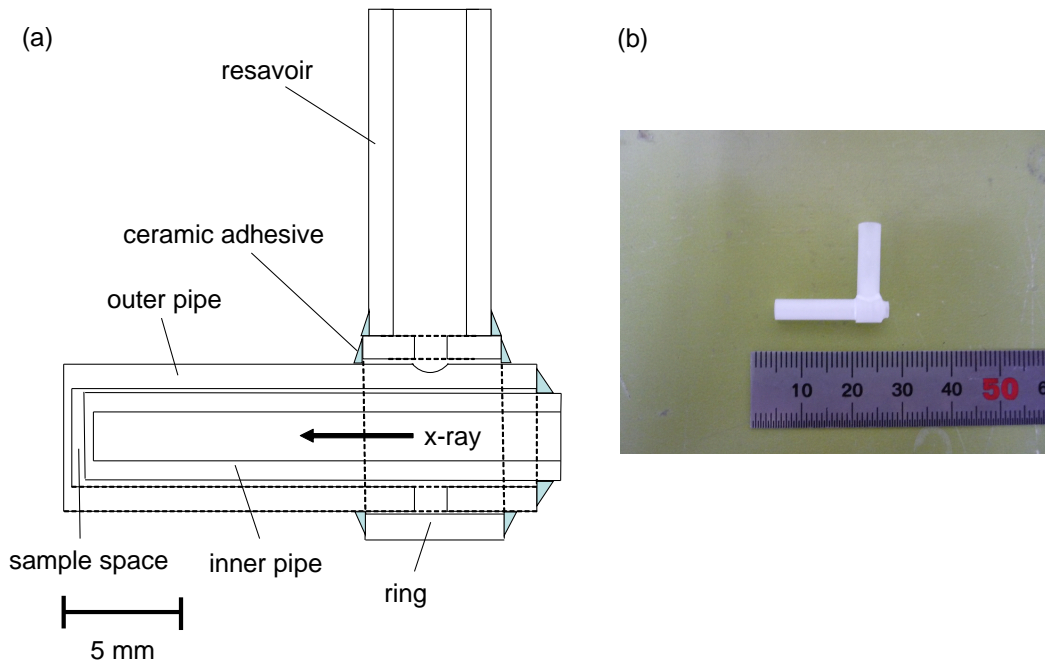


Figure 2.2: (a) Cross sectional diagram and (b) photograph of the sample cell

2.1.2 Sealing Test

In order to confirm that the sample cell is tightly sealed except for the opening of the reservoir, a sealing test of the cell was done [48]. As mentioned later, for introducing the sample into the cell, it is required that all parts are joined without the leakage of helium (He) gas.

Because the x-ray windows of the cell are fragile, special care is required in the sealing test to avoid the damage due to the difference of the pressures between the inside and the outside of the cell. Therefore, the sealing test was done as follows, and we confirmed that there was no leakage of He gas from the cell.

Figure 2.3 shows the setup for the sealing test. The setup consists of a vacuum bell jar, a brass stage, a He gas bag, a rotary pump, and a He leak detector. Two pipes pass through the brass stage as shown in the figure, and the cell is joined to the one of the pipes with the silicon tube. First, the bell jar and the cell are evacuated at the same time, by opening the main valve and valve V3, and closing the valves V1, V2, and V4. In this procedure, the pressures in the inside and outside of the cell are kept the same, which prevents the thin x-ray windows of the cell from being damaged owing to the difference of the pressures. Then, the valve V3 is closed and V4 is opened, so that the insides of the bell jar and the cell are evacuated with the turbo pump in the He leak detector. After the evacuation, the main valve is closed and the valves V1 and V2 are opened. If the cell is sealed, the He gas can not reach the He leak detector and the mass flow rate of the He gas does not change from the original value ($\sim 10^{-11}$ Pa m³ s⁻¹). Thus, we can confirm whether the cell is sealed or not.

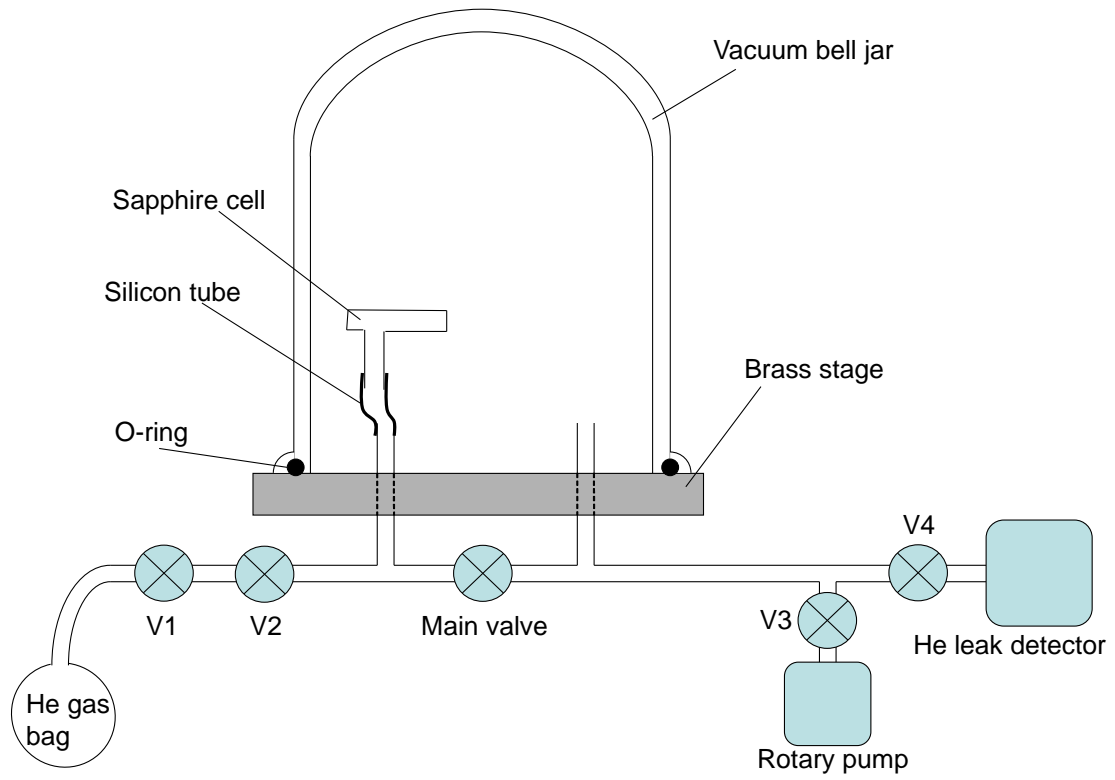


Figure 2.3: Setup for the sealing test of the sample cell.

2.2 Introduction of the Sample into the Cell

Figure 2.4 shows the setup for introducing the sample into the cell [48]. Because of the high reactivity of the alkali metals to the air, this procedure was done in a glove box filled with purified He gas. First, we put a sample injector, which consists of a piston and a cylinder, on the reservoir of the cell, as shown in Fig. 2.4. The solid sample was in this injector. Then, we evacuated the vacuum desiccator. In this procedure, the sample space of the cell was also evacuated. After the evacuation, we closed the valve V1, and began to heat the sample with a heater, which was coiled around a aluminum stage. When the sample was heated up to the melting point, the molten sample could not sustain the weight of the piston and the piston descended down. As a result, the sample was pushed out from the injector into the reservoir area. After this, we opened the valve V2 and introduced the He gas. The surface of the liquid sample in the reservoir was pushed by the He gas, and the sample reached to the sample space of the cell. Pressure imbalance between the sample space and the outside of the cell is essential for this procedure. If there were a leakage of the He gas in the cell, He gas would penetrate into the sample space, and the space would not be filled with the sample.

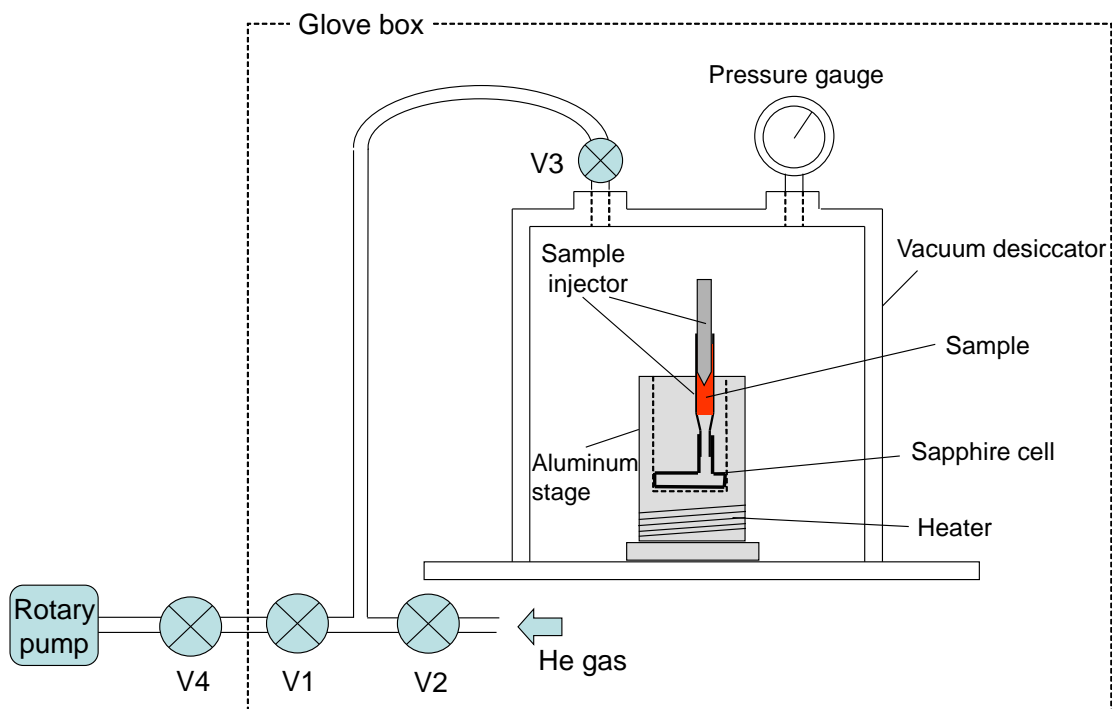


Figure 2.4: Setup for introducing the sample into the cell.

2.3 Chamber for Inelastic X-ray Scattering

Figures 2.5 (a), (b) show a schematic diagram and a picture of the chamber for the IXS measurements. We used kapton foils (thickness $50 \mu\text{m}$) for the x-ray windows of the chamber. After the sample introduction, the cell was set to the chamber as shown in Fig. 2.5 (a), and the chamber was sealed in the glove box. Then, we brought out the chamber from the glove box. We also set the heater and the thermocouples in the chamber.

Figure 2.6 shows the enlargement of the cell inserted into a furnace in the chamber. The furnace consists of a molybdenum (Mo) tube and a Fe-Cr heater. The Fe-Cr heater (diameter 0.40 mm) was fixed around the Mo tube. Thermocouples were inserted in the holes drilled in the Mo tube. Alumina tubes were used for the electrical insulation. For the heater, the inner and outer diameters of the alumina tube are 0.50 mm and 1.0 mm, respectively. For the thermocouples, we used the alumina tubes with two holes. The diameter of this hole is 0.30 mm, and the outer diameter of this alumina tube is 1.2 mm.

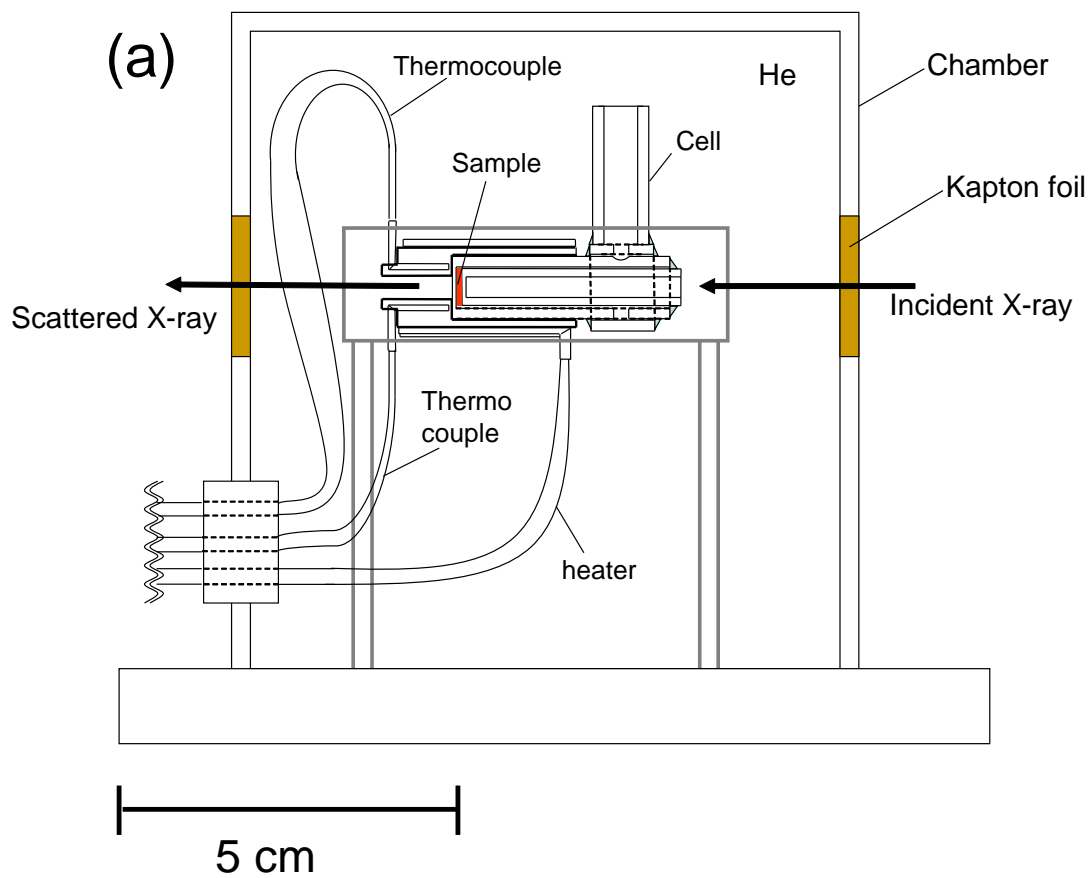


Figure 2.5: (a) Schematic drawing of the chamber for the IXS measurements. (b) Photograph of the chamber.

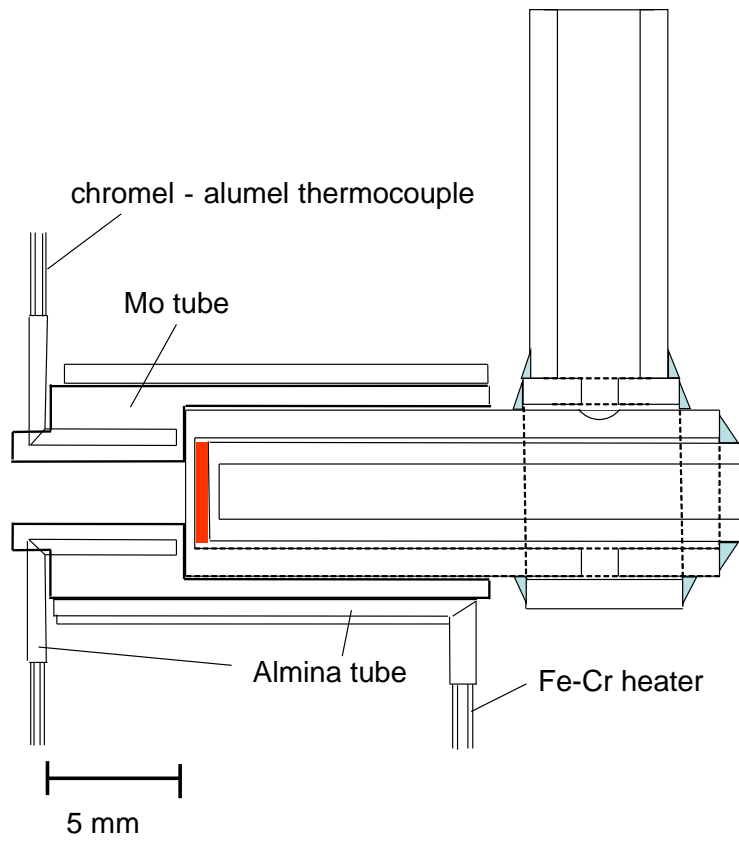


Figure 2.6: Furnace in the chamber for IXS measurements, into which the sample cell is inserted.

2.4 Inelastic X-ray Scattering Beamline

We have performed IXS experiments at the Taiwan inelastic x-ray scattering beamline BL12XU of SPring-8, which is designed for observing various electronic excitations [49]. Figure 2.7 shows the layout of the beamline. The incident beam from the undulator was monochromatized using a combination of Si (111) double crystal monochromator and a Si (400) four-crystal high-resolution monochromator. The energy resolution ~ 0.2 eV was obtained for the energy of the incident x-ray 13.8 keV. IXS was measured with a spherical crystal analyzer and a Si detector in a near backscattering geometry. The experiments were carried out in the so-called inverse geometry, where the scattered photon energy is fixed at a certain energy and the incident photon energy is scanned near that energy.

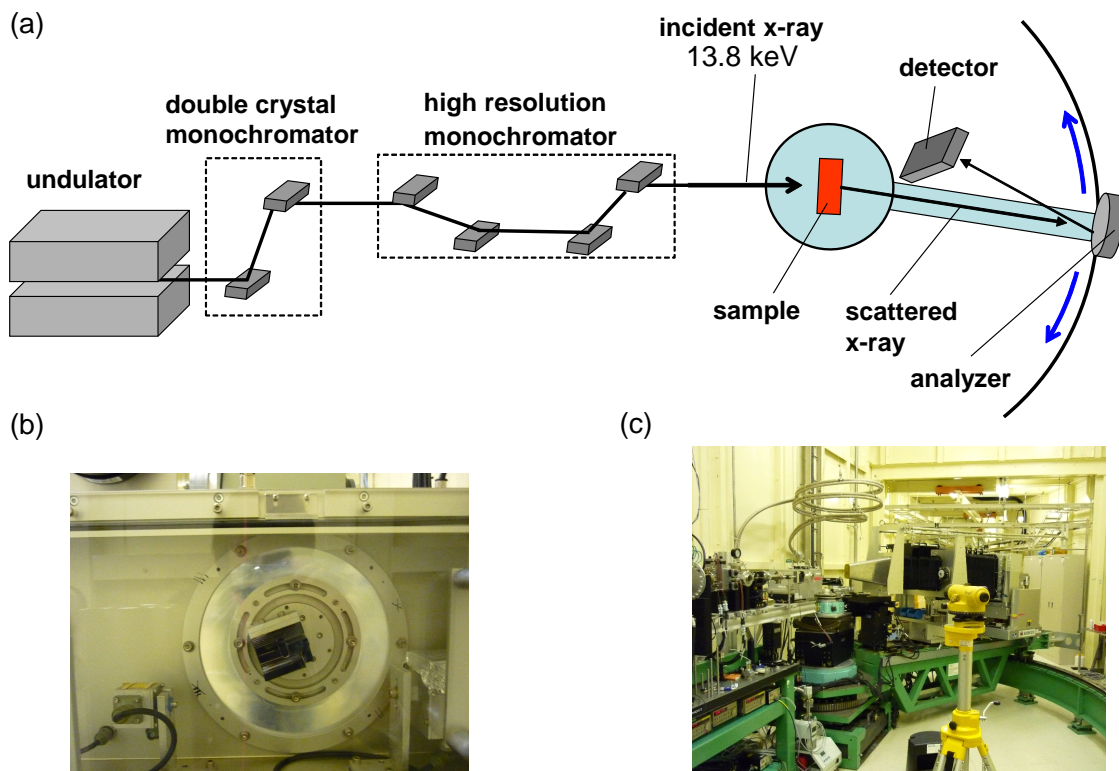


Figure 2.7: (a) Layout of the Taiwan inelastic x-ray scattering beamline BL12XU in SPring-8. (b) Picture of the high resolution monochromator. (c) Picture of the experimental hutch.

2.5 Experimental Conditions

2.5.1 Measurements for Rb

The IXS measurements were performed at room temperature for solid Rb, and at 333 K for liquid Rb. (The melting point of Rb is 312 K.) The range of the energy transfer, $\hbar\omega$, was from 0.5 eV to 6.5 eV. The range of the momentum transfer, q , was from 0.18 \AA^{-1} to 0.90 \AA^{-1} for solid Rb, and from 0.18 \AA^{-1} to 0.80 \AA^{-1} for liquid Rb respectively. The measurements took about 3 hours for each q , and the total counts at inelastic peak positions were ~ 100 [counts].

The thickness of the sample cell was adjusted to be $300 \mu\text{m}$. This value is determined as follows. The ratio of the intensity of the transmitted x-ray to the incident x-ray can be expressed as $\exp[-\mu t]$, where μ is the absorption coefficient and t is the thickness of the sample. On the other hand, the number of the scatterers is proportional to the thickness t . Therefore, the intensity of the scattered x-ray is proportional to the factor $t \exp[-\mu t]$, which takes the maximum at $t = 1/\mu (\equiv t_{\text{max}})$.

The density ρ_{M} of solid Rb, and the mass absorption coefficient μ_{M} of Rb for 13.8 keV [50] are

$$\rho_{\text{M}} = 1.53 \text{ g cm}^{-3}, \quad \mu_{\text{M}} = 24 \text{ cm}^2\text{g}^{-1}.$$

From these values the liner absorption coefficient $\mu = \rho_{\text{M}}\mu_{\text{M}}$ is estimated to be

$$\mu = 37 \text{ cm}^{-1}.$$

Thus t_{max} is calculated as

$$t_{\text{max}} \sim 270 \mu\text{m}.$$

Considering that the density becomes lower upon melting, we set the thickness as $300\mu\text{m}$.

2.5.2 Measurements for Cs

The IXS measurements were performed for liquid Cs at 313 K. (The melting point of Cs is 302 K.) The energy transfer was from 0.5 eV to 4.5 eV. The momentum transfer was from 0.32 \AA^{-1} to 0.55 \AA^{-1} . The measurements took about 9 hours in average for each q . The total counts at the inelastic peak position were ~ 100 [counts]. The thickness of the sample was adjusted to be $80 \mu\text{m}$. This value is determined from t_{max} for solid Cs, $74 \mu\text{m}$. The value of t_{max} is derived from the density ($\rho_{\text{M}} = 1.93 \text{ g cm}^{-3}$) and the mass absorption coefficient for 13.8 keV ($\mu_{\text{M}} = 70 \text{ cm}^2\text{g}^{-1}$ [50]) of solid Cs.

Chapter 3

Formulation of the Plasmon Line Width in Liquid Metals

Formulation for evaluating the plasmon line width in liquid metals is derived in this chapter. So far, the plasmon line width has been calculated mainly for the solid state [30, 31], where the effects of interband transitions, phonon-assisted intraband (or interband) transitions, and the excitations of two electron-hole (e-h) pairs are considered. The effects of phonon and two e-h pairs can be calculated without using information on the ionic structure [31]. Therefore, these effects are readily extended to the liquid systems. On the other hand, the effect of the interband transitions is strongly dependent on the ionic structure, and thus the extension of this effect to the liquid state is difficult relative to the other two effects.

In this chapter, we derive a formula for evaluating the plasmon line width at $q = 0$ in liquid metals. In addition, the application of the formula to the liquid alkali metals is shown [51].

3.1 Derivation of the Formula

The plasmon line width at $q = 0$, $\Delta E_{1/2}(0)$, is represented as [31]

$$\Delta E_{1/2}(0) = \hbar\omega_p \varepsilon_2(0, \omega_p), \quad (3.1)$$

where ε_2 is the imaginary part of the dielectric function. Therefore, the $\Delta E_{1/2}(0)$ can be calculated when the formula for $\varepsilon_2(0, \omega_p)$ is given. (Hereafter, we do not indicate the q dependence, if $q = 0$.) For the calculation of $\varepsilon_2(\omega_p)$, we use the following relations [52],

$$\varepsilon(\omega) = 1 + i \frac{4\pi\sigma(\omega)}{\omega}, \quad (3.2)$$

$$\text{Re}\sigma(\omega) = -\text{Im} \left[\frac{\pi(\omega)}{\omega} \right], \quad (3.3)$$

where $\sigma(\omega)$ is the conductivity and $\pi(\omega)$ is the retarded form of the current-current correlation function $\pi(i\omega)$. In the isotropic systems where the nearly-free-electron model is a good approximation, $\pi(i\omega)$ can be expressed as [52]

$$\begin{aligned} \pi(i\omega) = & \frac{1}{4\pi m^2 (i\omega)^2} \sum_{\mathbf{q}'} \frac{q'^4}{3} \left[\frac{1}{\varepsilon_{\text{EG}}(\mathbf{q}', i\omega)} - \frac{1}{\varepsilon_{\text{EG}}(\mathbf{q}', 0)} \right] \\ & \times \langle \Phi(\mathbf{q}') \Phi(-\mathbf{q}') \rangle, \end{aligned} \quad (3.4)$$

where $\varepsilon_{\text{EG}}(\mathbf{q}', \omega)$ is the dielectric function of the electron gas, and $\Phi(\mathbf{q}')$ describes the potential aside from electron-electron interaction [52]. For example, $\Phi(\mathbf{q}')$ can describe the potential of impurities $V_{\text{imp}}(\mathbf{q}')$. In this case $\Phi(\mathbf{q}')$ is written as $\Phi(\mathbf{q}') = \frac{V_{\text{imp}}(\mathbf{q}')}{\nu} \rho_{\text{imp}}(\mathbf{q}')$, where ν is the total volume and $\rho_{\text{imp}}(\mathbf{q}')$ is the density operator of impurities [52].

In the case of ionic potential in liquid, $\Phi(\mathbf{q}')$ can be represented as,

$$\Phi(\mathbf{q}') = \frac{V_{\text{ion}}(\mathbf{q}')}{\nu} \rho_{\text{ion}}(\mathbf{q}'), \quad (3.5)$$

$$V_{\text{ion}}(\mathbf{q}') = \int d^3r e^{i\mathbf{q}' \cdot \mathbf{r}} V_{\text{ion}}(\mathbf{r}), \quad \rho_{\text{ion}}(\mathbf{q}') = \sum_j e^{i\mathbf{q}' \cdot \mathbf{R}_j}, \quad (3.6)$$

where $V_{\text{ion}}(\mathbf{r})$ is the ionic potential and \mathbf{R}_j is the position of the j -th ion in liquid.

From Eq. (3.5), we obtain

$$\begin{aligned}\langle \Phi(\mathbf{q}')\Phi(-\mathbf{q}') \rangle &= \frac{1}{\nu^2} \langle V_{\text{ion}}(\mathbf{q}')V_{\text{ion}}(-\mathbf{q}') \rangle \langle \rho_{\text{ion}}(\mathbf{q}')\rho_{\text{ion}}(-\mathbf{q}') \rangle \\ &= \frac{n_{\text{ion}}}{\nu} V_{\text{ion}}(\mathbf{q}')^2 S(\mathbf{q}'),\end{aligned}\quad (3.7)$$

where n_{ion} is the ionic density and $S(\mathbf{q}')$ is the liquid structure factor defined by $n_{\text{ion}}\nu S(\mathbf{q}') = \langle \rho_{\text{ion}}(\mathbf{q}')\rho_{\text{ion}}(-\mathbf{q}') \rangle$. When we convert the summation into the integral in Eq. (3.4), $\sum_{\mathbf{q}'} \rightarrow \nu \int \frac{d^3q'}{(2\pi)^3}$, we obtain the following expression from Eqs. (3.2) - (3.4) and (3.7):

$$\begin{aligned}\text{Im}\varepsilon_2^{\text{ion}}(\omega) &= \frac{4}{3n_{\text{ion}}(\hbar\omega/E_{\text{F}})^4} \int \frac{d^3q'}{(2\pi)^3} \left(\frac{q'}{k_{\text{F}}}\right)^4 \\ &\quad \times \left| \frac{v_{\text{ion}}(\mathbf{q}')/\varepsilon_{\text{EG}}(\mathbf{q}',\omega)}{E_{\text{F}}} \right|^2 S(\mathbf{q}') \text{Im}[\varepsilon_{\text{EG}}(\mathbf{q}',\omega)],\end{aligned}\quad (3.8)$$

where $v_{\text{ion}} = n_{\text{ion}}V_{\text{ion}}$. When we derive Eq. (3.8), we use the relation $-\text{Im}[1/\varepsilon_{\text{EG}}] = \text{Im}\varepsilon_{\text{EG}}/|\varepsilon_{\text{EG}}|^2$. Finally, from Eqs. (3.1) and (3.8), the following formula is obtained:

$$\begin{aligned}\Delta E_{1/2}^{\text{ion}}(0) &= \hbar\omega_{\text{p}} \frac{4}{3n_{\text{ion}}(\hbar\omega_{\text{p}}/E_{\text{F}})^4} \int \frac{d^3q'}{(2\pi)^3} \left(\frac{q'}{k_{\text{F}}}\right)^4 \\ &\quad \times \left| \frac{v_{\text{ion}}^{\text{s}}(\mathbf{q}')}{E_{\text{F}}} \right|^2 S(\mathbf{q}') \text{Im}\varepsilon_{\text{EG}}(\mathbf{q}',\omega_{\text{p}}),\end{aligned}\quad (3.9)$$

where we neglect the ω dependence of the screening and write the screened potential as $v_{\text{ion}}^{\text{s}}(\mathbf{q}') (\equiv v_{\text{ion}}(\mathbf{q}')/\varepsilon_{\text{EG}}(\mathbf{q}',\omega=0))$.

It should be stressed that by setting $\Phi(\mathbf{q}') = \sum_{\mathbf{G}} V_{\text{ion}}(\mathbf{G})\delta_{\mathbf{q}'=\mathbf{G}}$ the equation

$$\begin{aligned}\Delta E_{1/2}^{\text{ion}}(0) &= \hbar\omega_{\text{p}} \frac{4}{3(\hbar\omega_{\text{p}}/E_{\text{F}})^4} \sum_{\mathbf{G}} \left(\frac{\mathbf{G}}{k_{\text{F}}}\right)^4 \\ &\quad \times \left| \frac{v_{\text{ion}}^{\text{s}}(\mathbf{G})}{E_{\text{F}}} \right|^2 \text{Im}\varepsilon_{\text{EG}}(\mathbf{G},\omega_{\text{p}})\end{aligned}\quad (3.10)$$

is derived [52], under the assumption that the system has a cubic symmetry [53]. Equation (3.10) describes the effect of interband transitions in crystalline systems [31]. Equation (3.9) is similar to Eq. (3.10). The difference between the two equa-

tions is how structural information is included. In Eq. (3.9), structural information is included in the structure factor $S(\mathbf{q}')$, whereas in Eq. (3.10) it is included in the reciprocal lattice vector \mathbf{G} .

Figures 3.1 (a), (b) schematically illustrate the mechanism of the plasmon damping at $q = 0$ described with Eqs. (3.10) and (3.9). For the solid state, if the reciprocal lattice vector is located within the electron-hole (e-h) continuum as shown in Fig. 3.1 (a), the e-h pair excitations occur at $q = 0$ through the Umklapp process, which causes the broadening of the plasmon line width in the long-wavelength limit. For the liquid state, on the other hand, the e-h pair excitations at each momentum transfer within the e-h continuum at $\hbar\omega = \hbar\omega_p$ contribute to the broadening of the line width at the long-wavelength limit, and the degree of the contribution at each q is determined by the liquid structure factor $S(q)$. The relation between the short range order and the finite plasmon line width in the liquid state has been discussed in the previous IXS studies for liquid samples [16, 33, 35], but has not been described in a quantitative manner. Equation (3.9) enables us to quantitatively describe the relation between the short range order of ions and the plasmon damping.

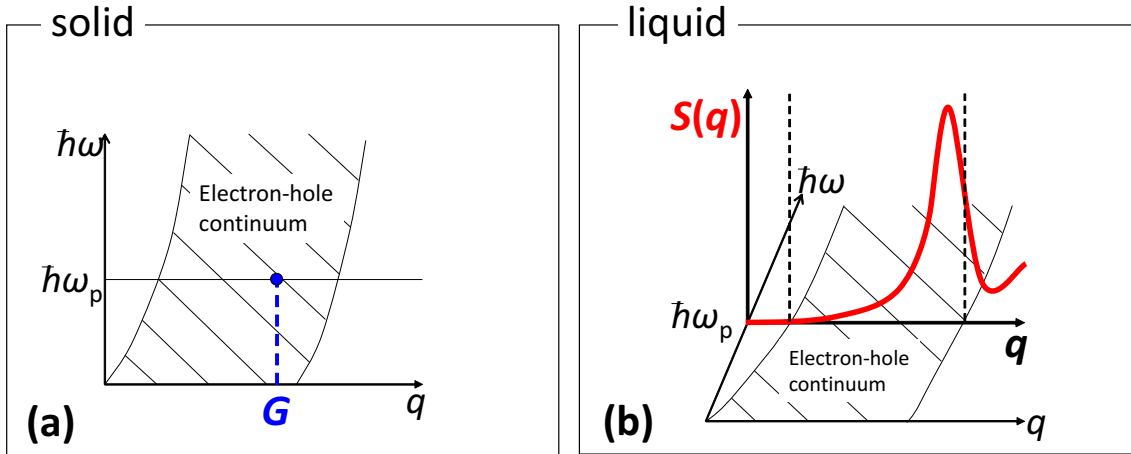


Figure 3.1: Schematic illustration of the mechanism of the plasmon damping at $q = 0$ in the (a) solid state (Eq. (3.10)) and the (b) liquid state (Eq. (3.9)).

3.2 Application of the Formula to Alkali Metals

The line widths of solid and liquid alkali metals are calculated, using Eqs. (3.10) and (3.9), in this section. To calculate the screened potential, $v_{\text{ion}}^{\text{s}}(\mathbf{q}') = v_{\text{ion}}(\mathbf{q}')/\varepsilon_{\text{EG}}(\mathbf{q}')$, in Eqs. (3.9) and (3.10), we use the the Lindhard dielectric function $\varepsilon_{\text{L}}(q')$

$$\varepsilon_{\text{L}}(q') = 1 + \frac{4\pi e^2 k_{\text{F}} m}{q'^2 \pi^2 \hbar^2} \times \left\{ \frac{1}{2} + \frac{4k_{\text{F}}^2 - q'^2}{8k_{\text{F}}q'} \ln \left| \frac{2k_{\text{F}} + q'}{2k_{\text{F}} - q'} \right| \right\}. \quad (3.11)$$

and the Ashcroft's empty core potential [54]

$$v_{\text{ion}}(q') = \frac{4\pi e^2 n_{\text{ion}}}{q'^2} \cos(q' R_{\text{core}}). \quad (3.12)$$

For Li, Na, K, Rb, and Cs in both the solid and liquid states, we set R_{core} as 1.06, [55] 0.96, [56] 1.20, [56] 1.38, [56] and 1.55 [56] Å, respectively. As $\text{Im}\varepsilon_{\text{EG}}(\mathbf{q}', \omega_{\text{p}})$ in Eqs. (3.9) and (3.10), we use the imaginary part of the Lindhard dielectric function ε_{L} for finite ω ,

$$\text{Im}\varepsilon_{\text{L}}(q', \omega) = \frac{\pi}{2} \frac{\hbar\omega}{\hbar q' v_{\text{F}}} \frac{k_{\text{TF}}^2}{k^2}, \quad \hbar\omega \leq \hbar q' v_{\text{F}} - E_{\text{F}} \quad (3.13)$$

$$= \frac{\pi}{4} \frac{k_{\text{F}}}{q'} \left[1 - \frac{(\hbar\omega - E_{\text{F}})^2}{\hbar^2 q'^2 v_{\text{F}}^2} \right] \frac{k_{\text{TF}}^2}{q'^2}, \quad \hbar q' v_{\text{F}} - E_{\text{F}} \leq \hbar\omega \leq \hbar q' v_{\text{F}} + E_{\text{F}} \quad (3.14)$$

$$= 0, \quad \hbar\omega \geq \hbar q' v_{\text{F}} + E_{\text{F}}, \quad (3.15)$$

where $v_{\text{F}} = \hbar k_{\text{F}}/m$, and $k_{\text{TF}} = \sqrt{3}\omega_{\text{p}}/v_{\text{F}}$. The values of n_{ion} from Li to Cs in the calculation are 0.046, 0.025, 0.013, 0.011, and 0.0087 for the solid state, and 0.044, 0.024, 0.013, 0.010, and 0.0083 for the liquid state. In Eq. (3.10), only \mathbf{G} along the [110] direction, \mathbf{G}_{110} , contributes to $\Delta E_{1/2}^{\text{ion}}(0)$ for solid alkali metals [31]. We set $|\mathbf{G}_{110}| = 2.55$ (Li), 2.10 (Na), 1.70 (K), 1.59 (Rb), and 1.47 (Cs) Å⁻¹. The $S(q')$ used in the calculations for the liquid state is taken from the experimental results of Franz *et al.* [57] for Rb and of Waseda [58] for the other elements.

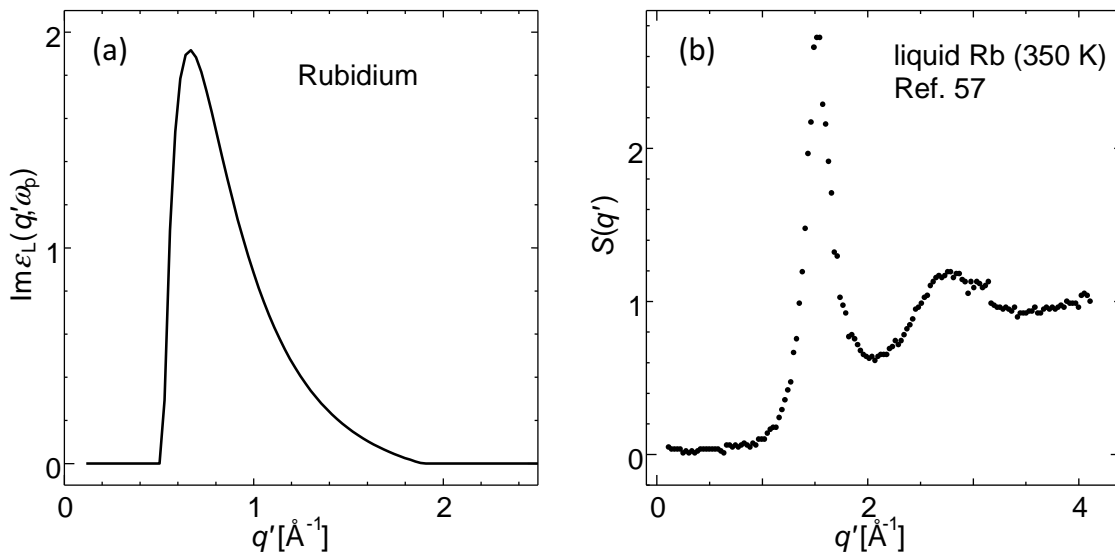


Figure 3.2: (a) Imaginary part of the Lindhard dielectric function (Eq. (3.13)) at $\omega = \omega_p$ as a function of q' in the case of Rb. (b) Structure factor of liquid Rb at 350 K taken from the experimental work by Franz *et al.* [57].

Figure 3.2 (a) shows the q' dependence of $\text{Im}\varepsilon_L(q', \omega)$ at $\omega = \omega_p$ in the case of Rb. The range where $\text{Im}\varepsilon_L(q', \omega_p)$ has finite values corresponds to the q' range within the e-h continuum. Figure 3.2 (b) shows the liquid structure factor of Rb at 350 K [57], which is used in the calculation.

We also consider the effect of phonons, $\Delta E_{1/2}^{\text{ph}}(0)$, which can be evaluated by [31]

$$\Delta E_{1/2}^{\text{ph}}(0) = \frac{\hbar}{\tau}, \quad \tau = \frac{m}{\rho n e^2}, \quad (3.16)$$

where ρ is the electrical resistivity and n is the electronic density, which is equal to n_{ion} in the alkali metals. As the values of ρ , the electrical resistivity at 273 K [59] and that at the melting point [60] are used in the solid and liquid states, respectively.

Table 3.1 shows the results of the calculation. We find that the ionic contribution $\Delta E_{1/2}^{\text{ion}}(0)$ becomes smaller upon melting for these elements. This means that the effect of the ionic potential on plasmon damping is smaller in the liquid state than in the solid state. This reduction in $\Delta E_{1/2}^{\text{ion}}(0)$ originates from the variation in ionic structure upon melting. On the other hand, the contribution from phonons, $\Delta E_{1/2}^{\text{ph}}(0)$, becomes larger upon melting, which reflects the enhancement of thermal

motion. However, $\Delta E_{1/2}^{\text{ph}}(0)$ is much smaller than $\Delta E_{1/2}^{\text{ion}}(0)$, and thus the sum of these two terms, $\Delta E_{1/2}(0) = \Delta E_{1/2}^{\text{ion}}(0) + \Delta E_{1/2}^{\text{ph}}(0)$, decreases upon melting for all these elements. It should also be pointed out that the values of $\Delta E_{1/2}(0)$ for solid and liquid Li are much larger than those for the other elements, although $\Delta E_{1/2}(0)$ decreases as the atomic number reduces from Cs to Na. This result is attributed to the larger pseudopotential of Li relative to the other alkali metals.

Table 3.1: Calculated results of the plasmon line width in alkali metals at $q = 0$, $\Delta E_{1/2}(0)$, in the solid and liquid states. The ionic and phonon parts are also shown, which are denoted as ‘ion’ and ‘ph’, respectively. The values in parentheses are obtained by extrapolating the IXS results to $q = 0$. We use our data for Rb [61] (see Chapter 4) and the data of Hill *et al.* [16] for Li.

	solid			liquid		
	$\Delta E_{1/2}(0)$	ion	ph	$\Delta E_{1/2}(0)$	ion	ph
Li	1.16 (1.8 \pm 0.4)	1.09	0.074	1.00 (1.6 \pm 0.4)	0.80	0.20
Na	0.25	0.23	0.021	0.19	0.15	0.043
K	0.28	0.26	0.016	0.20	0.17	0.031
Rb	0.44 (0.47 \pm 0.07)	0.42	0.022	0.31 (0.27 \pm 0.13)	0.27	0.043
Cs	0.54	0.51	0.031	0.47	0.41	0.056

Table 3.1 also shows the experimentally obtained values of $\Delta E_{1/2}(0)$ in the solid and liquid states, in parentheses. At present, experimental values of $\Delta E_{1/2}(0)$ in the liquid alkali metals can be estimated for Li and Rb, using the data of the IXS study by Hill *et al.* [16] and of our IXS experiments for Rb [61] (see Chapter 4). The experimental values of $\Delta E_{1/2}(0)$ are derived by extrapolating the IXS results in the finite q region to the long-wavelength limit ($q = 0$). For Rb, the calculated results agree well with the experimental values, which demonstrates the validity of our formulation. For Li, it seems that the experimentally obtained $\Delta E_{1/2}(0)$ tends to decrease upon melting. This tendency is confirmed in the calculation. On the other hand, agreement with the experimental results is not quantitative for solid Li and liquid Li, that is, the calculated $\Delta E_{1/2}(0)$ is smaller than the experimental results. This deviation is probably attributed to the inadequacy of the Ashcroft’s empty core potential for Li [62].

Chapter 4

Plasmons in Liquid Rb

Previous EELS experiments on solid alkali metals [20] revealed that the plasmon dispersions in solid Rb and Cs significantly deviate from the prediction of the interacting electron gas model [21, 63]. To explain these deviations, *ab initio* calculations of plasmon dispersions in heavy alkali metals [28, 29] were performed, and it was shown that the band structure effect, especially the effect of the unoccupied *d*-states, strongly modifies the plasmon dispersion of solid Rb and Cs. According to the theoretical work by Jank *et al.* [14], the unoccupied *d*-states of Rb and Cs substantially change upon melting. Thus, comparison of the plasmon behaviors in the solid state with those in the liquid state will provide valuable information on how the band structure effect contributes to the plasmon dispersions in heavy alkali metals.

In this chapter, the IXS spectra of solid and liquid Rb [61] are presented. The plasmon dispersion relations and the line width are derived from these IXS spectra, and variation in the plasmon behavior upon melting is discussed.

4.1 Results

4.1.1 Raw IXS Spectrum

Figures 4.1 and 4.2 show the raw IXS spectra of solid and liquid Rb. The scattering angles and the corresponding q , where the IXS measurements were performed, are summarized in Table 4.1. The peak arising from plasmon is clearly seen for each

q at about 13838.8 eV (Fig. 4.1) for solid Rb, and 18839.0 eV for liquid Rb (Fig. 4.2). The the high intensity around 13836 eV is due to the quasielastic scattering contribution.

Table 4.1: The scattering angles and the corresponding momentum transfers q at which the measurements were performed. (* only solid Rb)

$2\theta[^\circ]$	1.48	2.30	2.96	3.69	4.10	4.52	4.93	5.34	5.74	6.57	7.40*
$q [\text{\AA}^{-1}]$	0.18	0.28	0.36	0.45	0.50	0.55	0.60	0.65	0.70	0.80	0.90

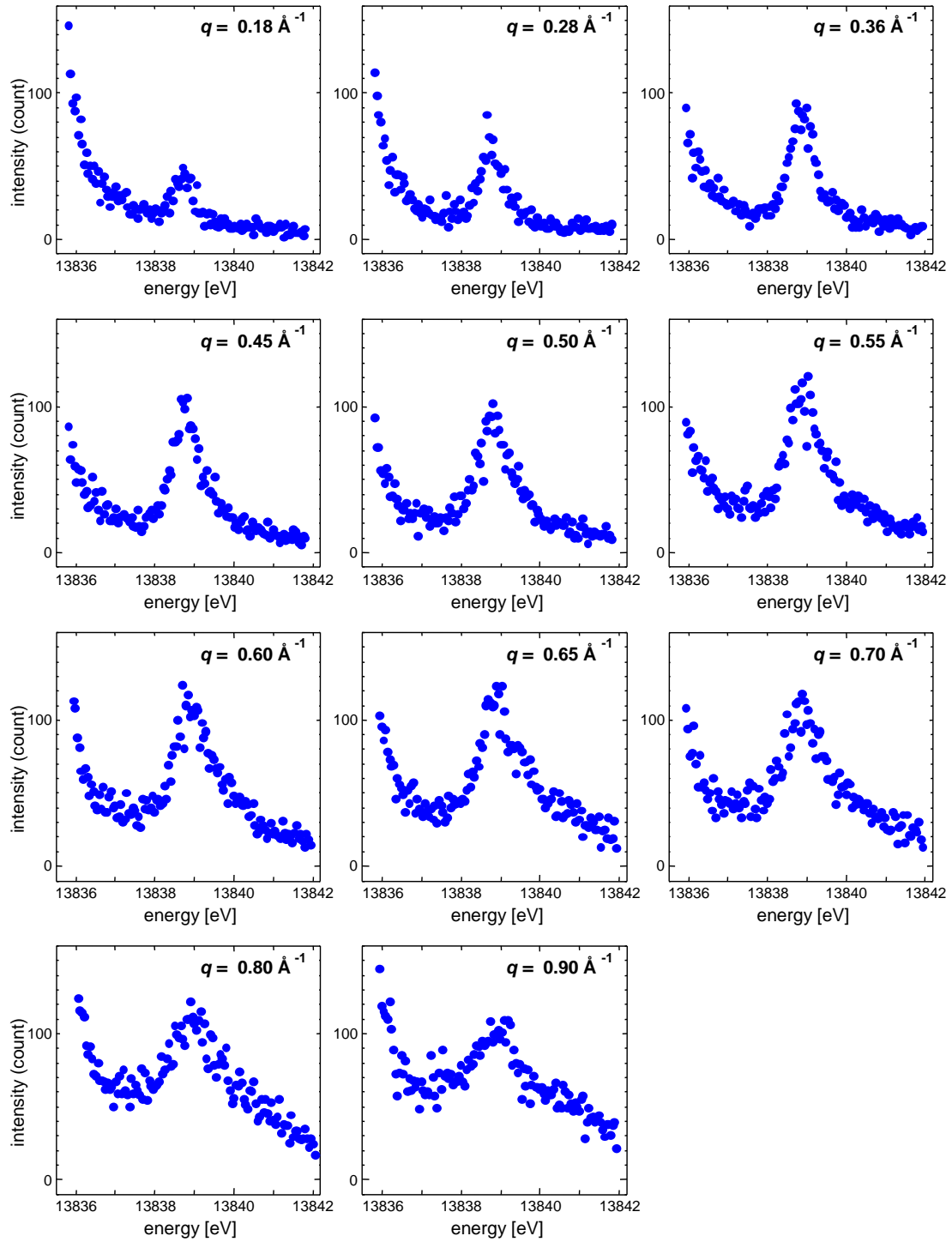


Figure 4.1: Raw IXS spectra of solid Rb. The horizontal axes correspond to the energy of the scattered x-ray. The vertical axes are the total counts. The momentum transfers are denoted as q .

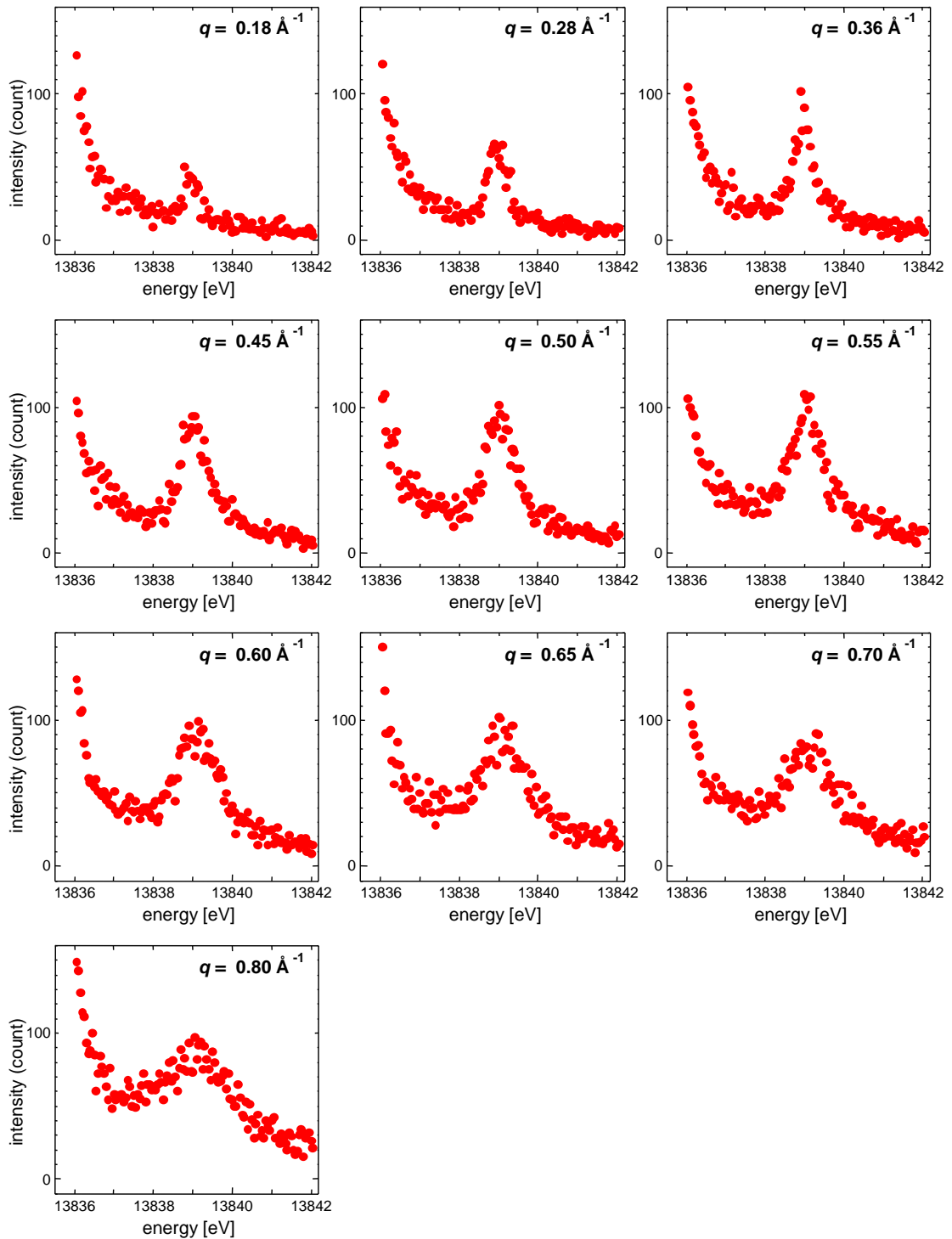


Figure 4.2: Raw IXS spectra of liquid Rb. The horizontal axes correspond to the energy of the scattered x-ray. The vertical axes are the total counts. The momentum transfers are denoted as q .

4.1.2 Data Analysis

The energy transfer $\hbar\omega$ is determined by subtracting the energy of the quasielastic scattering from that of the scattered x-ray. Figure 4.3 (a) shows the spectra of the quasielastic peaks, and Fig. 4.3 (b) shows the temporal variation in the incident beam intensity. As shown in Fig. 4.3 (b), the intensity of the incident beam tended to become weaker with time, and thus we readjusted the monochromators in the beamline, in order to restore the intensity of the incident beam. Because of this adjustment, the position of the quasielastic peak slightly moved. Therefore, measurements for the quasielastic scattering were performed after the readjustments. The readjustments were done two times during the beam time. This is why three quasielastic peaks (labeled No. 1, 2, 3) are shown in Fig. 4.3 (a). The peak positions were precisely evaluated with the Gaussian fitting. In addition, the energy resolution was estimated to be 0.22 eV from the full width at half maximum (FWHM) of the Gaussian. Table 4.2 summarizes the results of the fitting.

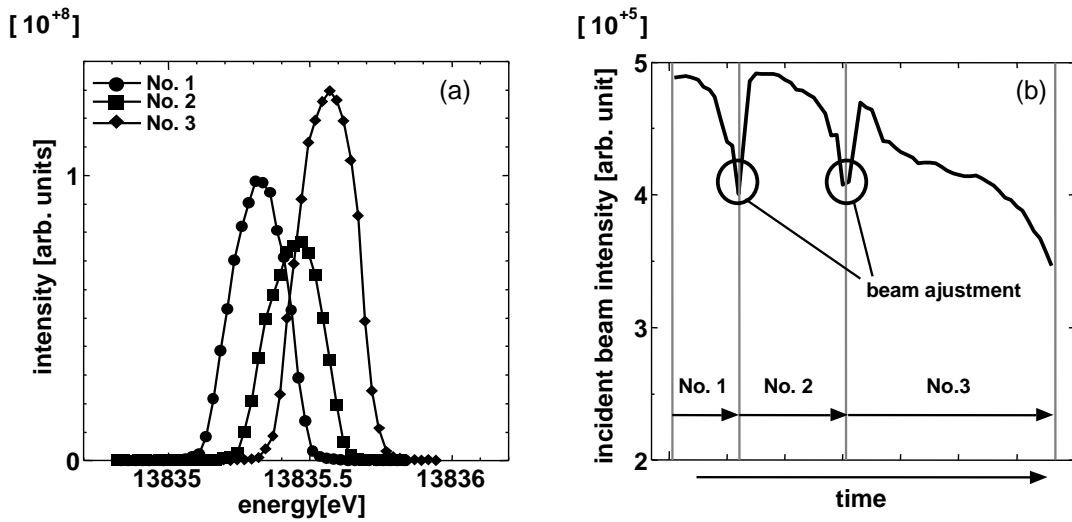


Figure 4.3: (a) Quasielastic peaks of Rb. (b) Temporal variation in the intensity of the incident x-ray.

Table 4.2: The results of Gaussian fitting to the quasielastic peaks. (FWHM = full width at half maximum)

	No. 1	No. 2	No. 3
peak position [eV]	13835.318 ± 0.002	13835.446 ± 0.002	13835.561 ± 0.002
FWHM [eV]	0.215 ± 0.004	0.217 ± 0.005	0.222 ± 0.006
peak height	3090 ± 49	2430 ± 44	4160 ± 80

Figure 4.4 shows the IXS spectra of the empty cell and the sample in the cell. The horizontal axis is the energy transfer $\hbar\omega$ and the vertical axis is normalized by the incident beam intensity. We can see that the inelastic signals from the empty cell are negligible compared to the sample, and thus we do not take into account the contribution of the empty cell.

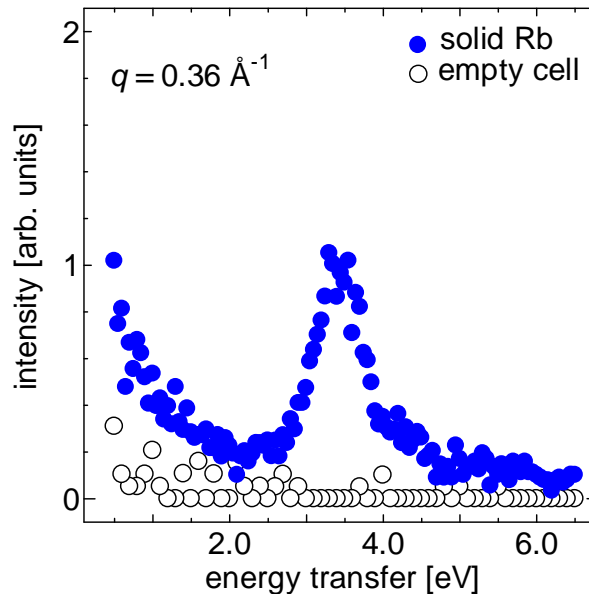


Figure 4.4: IXS spectra of solid Rb and the empty cell at $q = 0.36 \text{ \AA}^{-1}$.

Figures 4.5 (a), (b) show the IXS spectra of solid and liquid Rb as a function of $\hbar\omega$, respectively. These spectra are normalized by the incident beam intensity. The peaks due to plasmon are observed at about $\hbar\omega \sim 3.5 \text{ eV}$ in the spectra of both solid and liquid Rb for each q . The IXS spectra are fitted by the sum of the two Lorentzians [64] which are convoluted with Gaussian. The two Lorentzians represent the quasielastic and the inelastic contributions, respectively. The FWHM

of the Gaussian is set to the energy resolution 0.22 eV. The fitting functions are denoted by the solid curves in Fig. 4.5. The vertical lines in these figures show the inelastic peak positions at $q = 0.18 \text{ \AA}^{-1}$. Note that the inelastic peak position of liquid Rb shifts to larger energy region from the vertical line with increasing q than that of solid Rb beyond $q \sim 0.60 \text{ \AA}^{-1}$.

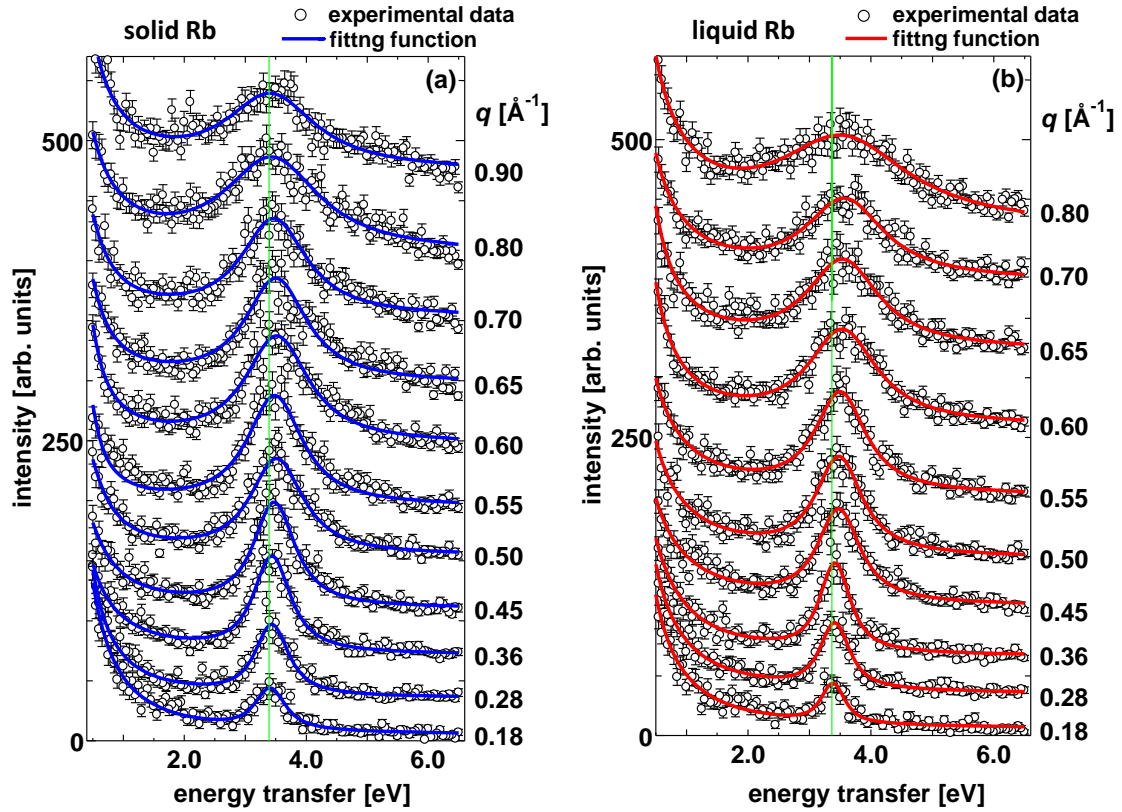


Figure 4.5: IXS spectra of (a) solid Rb and (b) liquid Rb normalized by the incident-beam intensity. Solid curves indicate the fitting function. The values at the right side of each figure are the momentum transfers. The vertical line indicates the peak position of the spectrum at $q = 0.18 \text{ \AA}^{-1}$.

4.1.3 Fitting Results

Figure 4.6 (a) shows the plasmon dispersions of solid and liquid Rb, derived from the fitting procedure. The cusp-like shape of the dispersion curve is observed for solid Rb, that is, with increasing q the plasmon energy gradually increases for $0.18 \text{ \AA}^{-1} \leq q \leq 0.50 \text{ \AA}^{-1}$, and then decreases within the range $0.60 \text{ \AA}^{-1} \leq q \leq 0.90 \text{ \AA}^{-1}$. This behavior is in agreement with the results of the EELS study [20]. On the other hand, the plasmon energy of liquid Rb monotonically increases with q . Within the range $q \geq 0.60 \text{ \AA}^{-1}$, the plasmon energy of liquid Rb becomes larger than that of solid Rb.

The dotted line in Fig. 4.6 (a) denotes the boundary of the electron-hole (e-h) continuum. This boundary was derived from Eq. (1.5) in Chapter 1. The experimentally determined plasmon dispersions intersect the dotted line at about $q \sim 0.50 \text{ \AA}^{-1}$. Thus, the plasmon cut-off wave vector q_c^{exp} is evaluated to be $q_c^{\text{exp}} \sim 0.50 \text{ \AA}^{-1}$.

Figure 4.6 (b) shows the q dependence of the plasmon line width $\Delta E_{1/2}(q)$, which is determined from the FWHM of Lorentzian curve in the fitting function. The line width $\Delta E_{1/2}(q)$ tends to be smaller in liquid Rb than in solid Rb within the range $q < q_c^{\text{exp}}$. In $q > q_c^{\text{exp}}$, on the other hand, $\Delta E_{1/2}(q)$ of liquid Rb tends to be larger than that of solid Rb. This tendency is observed more clearly in the inset of Fig. 4.6 (b), which shows the difference of $\Delta E_{1/2}(q)$ between solid and liquid Rb ($\Delta E_{1/2}^{\text{liq}}(q) - \Delta E_{1/2}^{\text{sol}}(q)$).

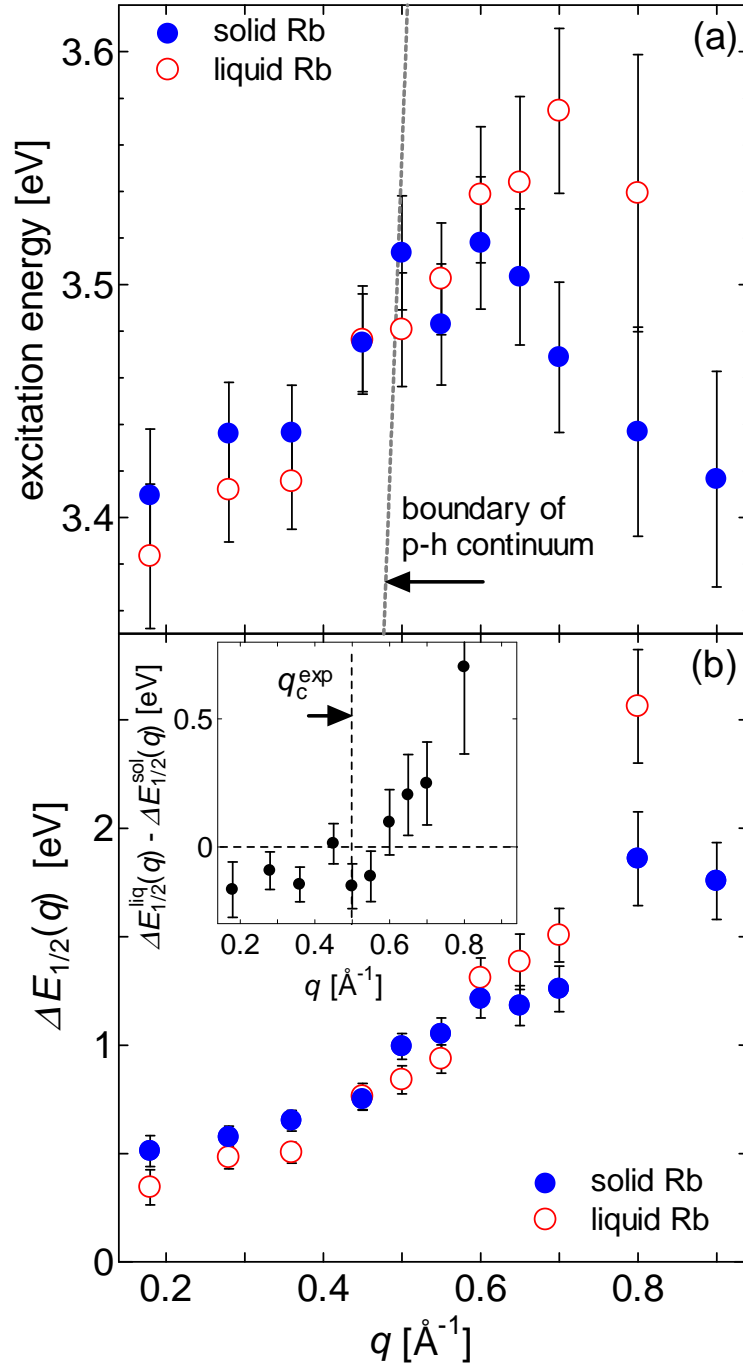


Figure 4.6: (a) Plasmon dispersions of solid and liquid Rb. The boundary of the electron-hole (e-h) continuum is indicated by the dotted line. (b) q dependence of the plasmon line width $\Delta E_{1/2}(q)$ of solid and liquid Rb. The inset shows the difference of $\Delta E_{1/2}(q)$ between solid and liquid Rb.

4.2 Discussion

4.2.1 Excitation Energy

In the previous theoretical study [28], it has been shown that the interband transitions to the unoccupied d -states strongly modify the plasmon dispersion in solid Rb. Therefore, we discuss the unoccupied DOS of solid and liquid Rb, to understand the origin of the observed variation in the plasmon dispersion upon melting.

Figure 4.7 shows theoretical DOS for solid [65] and liquid [66] Rb. The DOS of solid Rb is obtained by the full-potential LMTO (linear muffin-tin orbital) calculations for 300 K, which were carried out by Söderlind and Ross [65]. The DOS of liquid Rb is the result of the Schommers-LMTO-recursion method for 373 K, which was performed by Mirzoev *et al.* [66]. The total DOS is denoted with the solid curves, and the contribution from the d -states is shown with dashed curve. The DOS of free electrons is also shown by the thin solid curve. The shaded area indicates the energy range where the plasmons are observed in the IXS experiments.

The deviation from the DOS of free electrons is seen for that of solid Rb, where peaks are observed at about 1 eV, 2.5 eV, 4 eV and 5 eV. These peaks are mainly due to the d -state contribution. Upon melting, the peaks at about 4 eV and 5 eV are smoothed out. In addition, the broad peak at about 1.7 eV appears in the DOS of liquid Rb, instead of the sharp peaks at about 1 eV and 2.5 eV for the solid state.

The peaks in the unoccupied DOS modify the plasmon energy for the following reason. The enhancement of interband transitions owing to the peak in DOS at a certain energy makes the value of the imaginary part of the dielectric function $\varepsilon_2(\mathbf{q}, \omega)$ larger at that energy. The increase in $\varepsilon_2(\mathbf{q}, \omega)$ modifies the real part of the dielectric function, $\varepsilon_1(\mathbf{q}, \omega)$, through the Kramers-Kronig relation,

$$\varepsilon_1(\mathbf{q}, \omega) = 1 + \frac{2}{\pi} \int_0^\infty d\omega' \frac{\omega' \varepsilon_2(\mathbf{q}, \omega')}{\omega'^2 - \omega^2}. \quad (4.1)$$

Therefore, the plasmon energy is modified, because it is derived from the root of $\varepsilon_1(\mathbf{q}, \omega) = 0$.

In the previous theoretical work, Aryasetiawan *et al.* [28] discussed how interband transitions modify the plasmon energy. According to their discussion, plasmon energy is lowered if interband transitions are enhanced above the plasmon energy. To explain this lowering, they separated the integration range in the last term in eq. (4.1) into $[0, \omega_p^0]$ and $[\omega_p^0, \infty]$. Here, ω_p^0 is the plasmon energy, which is obtained without considering the enhancement of the interband transitions. At $\omega = \omega_p^0$, the term with the integration range $[\omega_p^0, \infty]$ positively contributes to $\varepsilon_1(\mathbf{q}, \omega)$. Thus, if interband transitions are enhanced within the range $\omega' > \omega_p^0$ and $\varepsilon_2(\mathbf{q}, \omega')$ increases in this range, the value of $\varepsilon_1(\mathbf{q}, \omega)$ increases at $\omega = \omega_p^0$. The increase in $\varepsilon_1(\mathbf{q}, \omega)$ at $\omega = \omega_p^0$ causes the lowering of the plasmon energy from ω_p^0 [28], because of the fact that the slope of ε_1 as a function of ω is generally positive at the plasmon energy.

Figure 4.8 illustrates the lowering of the plasmon energy described above. When the real part of the dielectric function at $\omega = \omega_p^0(q)$ increases from $\varepsilon_1^0(q, \omega_p^0)$ to $\tilde{\varepsilon}_1^0(q, \omega_p^0)$ owing to the interband transitions above ω_p^0 , plasmon energy becomes lower from $\omega_p^0(q)$ to $\tilde{\omega}_p(q)$.

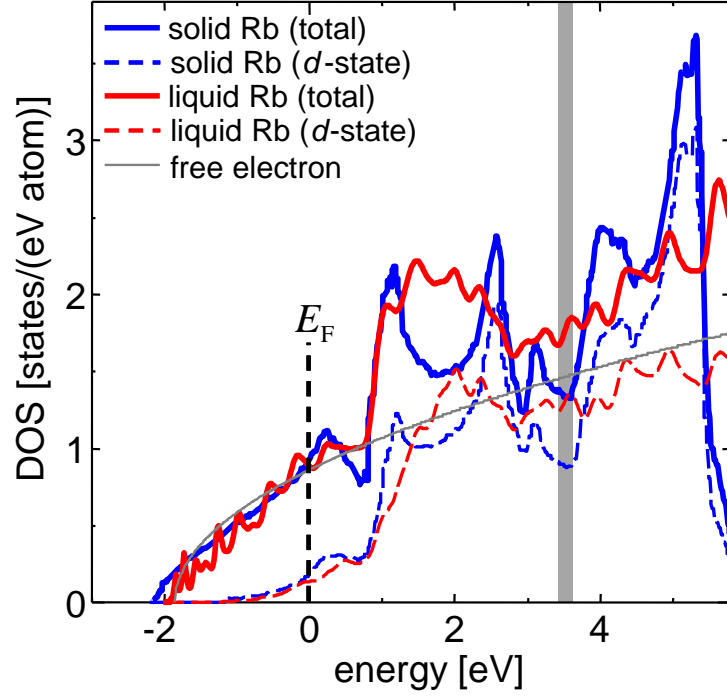


Figure 4.7: Theoretical density of states (DOS) of solid (300 K) [65] and liquid (373 K) [66] Rb. Solid and dashed lines show the total DOS and the contribution from d -states, respectively. Thin solid line shows the DOS of free electrons corresponding to the electron density of Rb. Shaded area shows the energy range where plasmon peaks were observed in the IXS measurements. The Fermi energy E_F is set to 0.

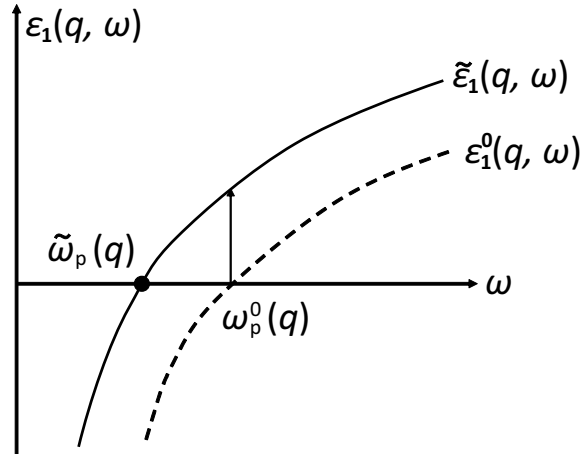


Figure 4.8: Schematic illustration of the lowering of plasmon energy due to the band structure effect. $\omega_p^0(q)$ and $\varepsilon_1^0(q, \omega)$ are the plasmon energy and the real part of the dielectric function, which are obtained without considering the enhancement of the interband transitions. $\tilde{\omega}_p(q)$ and $\tilde{\varepsilon}_1(q, \omega)$ are those including the enhancement of the interband transitions above $\omega_p^0(q)$.

In the DOS of liquid Rb, peaks are not clearly observed above the shaded area in Fig. 4.7. On the other hand, the peaks due to d -states are observed in the DOS of solid Rb at about 4 eV and 5 eV, the energies higher than the shaded energy range. Therefore, from the above discussion, the plasmon energy of solid Rb should be lowered more strongly than in liquid Rb, for the momentum transfer at which the s - d transitions are allowed. The probability of the s - d transitions becomes larger with increasing momentum transfer [28], and thus the lowering of the plasmon energy for solid Rb due to the interband transitions should be more evident for larger q . This q dependence of the s - d transitions qualitatively explains the observation that the plasmon energy of solid Rb is lower than that of liquid Rb for large q region (Fig. 4.6(a)). Therefore, we attribute the observed variation in the plasmon energy upon melting to the reduction of the band structure effect. In addition, it is suggested that the cusp-like dispersion in solid Rb originates from the band structure effect.

In the range of $q \leq 0.50 \text{ \AA}^{-1}$, the plasmon dispersion of solid Rb is in good agreement with that of liquid Rb as seen from Fig. 4.6 (a), which suggests that the band structure effect is not very important in this q range. For the quantitative comparison of the plasmon dispersions in both states within $q \leq 0.50 \text{ \AA}^{-1}$, we fitted the quadratic function of q , $\hbar\omega_p(q) = \hbar\omega_p(0)(1 + \alpha(\hbar^2/m)q^2)$, to the dispersion curve in the range of $q \leq 0.50$ ($\sim q_c^{\text{exp}}$). The results of the fitting are shown in Table 4.3. The value of α for solid Rb agrees with that for liquid Rb. On the other hand, the value of $\hbar\omega_p(0)$ for liquid Rb is slightly lower than that for solid Rb, which can be explained by the decrease in the density upon melting. The $\hbar\omega_p(0)$ is represented as $\hbar\omega_p(0) = \hbar\sqrt{4\pi n e^2 / m \varepsilon_B}$, $\varepsilon_B = 1 + 4\pi n_i \chi_i$, where n is the electron density, n_i is the ionic density and χ_i is the ionic polarizability. The value of χ_i was estimated by Mayer *et al.* [67] to be $1.5 \times 10^{23} \text{ cm}^3$. The density of solid Rb is 1.53 g cm^{-3} and that of liquid Rb is 1.46 g cm^{-3} . Using these values, $\hbar\omega_p(0)$ of solid and liquid Rb are calculated as 3.52 eV and 3.47 eV, respectively. From this estimation, the ratio of the value of $\hbar\omega_p(0)$ for liquid Rb to that for solid Rb is calculated as 0.986, which reasonably explains the experimental value 0.994 ± 0.008 .

Table 4.3: Experimental values of the plasmon energy at $q = 0$ ($\hbar\omega_p(0)$) and the plasmon dispersion coefficient α .

	Solid Rb (RT)	Liquid Rb (333 K)
$\hbar\omega_p(0)$ [eV]	3.39 ± 0.02	3.37 ± 0.02
α	0.06 ± 0.02	0.06 ± 0.02

4.2.2 Line Width

As mentioned in the previous section, the plasmon line width $\Delta E_{1/2}(q)$ of liquid Rb tends to be larger than that of solid Rb for $q > q_c^{\text{exp}}$ (inset of Fig. 4.6 (b)). Considering that a plasmon decays into an e-h pair for $q > q_c^{\text{exp}}$, it is suggested that the decay into an e-h pair is stronger in the liquid state than in the solid state. Such an enhanced damping in the liquid state is consistent with the increase in the DOS upon melting within the energy range where the plasmon is observed (shaded area in Fig. 4.7).

For $q < q_c^{\text{exp}}$, on the other hand, $\Delta E_{1/2}(q)$ tends to be smaller in liquid Rb than in solid Rb (inset of Fig. 4.6 (b)). In order to understand this tendency, we calculated the line width at $q = 0$, $\Delta E_{1/2}(0)$, for both solid and liquid Rb. The calculations were done using following equations, Eqs. (4.2) - (4.5).

The line width can be written as the sum of the ion part ($\Delta E_{1/2}^{\text{ion}}(0)$) and the phonon part ($\Delta E_{1/2}^{\text{ph}}(0)$),

$$\Delta E_{1/2}(0) = \Delta E_{1/2}^{\text{ion}}(0) + \Delta E_{1/2}^{\text{ph}}(0). \quad (4.2)$$

For solid Rb, $\Delta E_{1/2}^{\text{ion}}(0)$ is written as [31]

$$\begin{aligned} \varepsilon_2^{\text{ion}}(0, \omega_p) &= \frac{4n_{110}|v_s(G_{110})/E_F|^2(G_{110}/k_F)^4}{3(\hbar\omega_p/E_F)^4} \\ &\times \text{Im}\varepsilon_L(G_{110}, \omega_p), \quad (\text{for solid}) \end{aligned} \quad (4.3)$$

where G_{110} is the reciprocal lattice vector along the [110] direction, n_{110} is the number of the reciprocal lattice vectors equivalent to G_{110} , $v_s(q')$ is the Fourier component

of screened pseudopotential and $\varepsilon_L(q', \omega)$ is the Lindhard dielectric function. For liquid Rb, $\Delta E_{1/2}^{\text{ion}}(0)$ is represented as [51]

$$\begin{aligned} \varepsilon_2^{\text{ion}}(0, \omega_p) &= \frac{4}{3n_i(\hbar\omega_p/E_F)^4} \int \frac{d^3q'}{(2\pi)^3} \left(\frac{q'}{k_F}\right)^4 \\ &\quad \times \left| \frac{v_s(q')}{E_F} \right|^2 S(q') \text{Im}\varepsilon_L(q', \omega_p), \end{aligned} \quad (4.4)$$

(for liquid)

where $S(q')$ is the liquid structure factor. The effect of phonons $\Delta E_{1/2}^{\text{ph}}(0)$ is written as [31]

$$\Delta E_{1/2}^{\text{ph}}(0) = \frac{\hbar}{\tau}, \quad \tau = \frac{m}{\rho n e^2}, \quad (4.5)$$

where ρ is the electrical resistivity and n is the electronic density. The details of the calculations are given in Chapter 3.

Figure 4.9 shows the experimentally obtained plasmon line widths of solid and liquid Rb for small q region, which are indicated by circles. The calculated results at $q = 0$ are also shown in the same figure with diamonds for both the solid and liquid states. The dashed lines indicate the fitting functions to the experimental results (the quadratic function of q). The results of the calculation are in good agreement with the extrapolated values at $q = 0$ for both solid and liquid Rb.

Table 4.4 shows experimental and calculated values of $\Delta E_{1/2}(0)$, which are denoted as $\Delta E_{1/2}^{\text{exp}}(0)$ and $\Delta E_{1/2}^{\text{calc}}(0)$, respectively. The values of $\Delta E_{1/2}^{\text{ion}}(0)$ and $\Delta E_{1/2}^{\text{ph}}(0)$ in Eq. (4.2) are also indicated in the same table. We can see that $\Delta E_{1/2}^{\text{ph}}(0)$ of liquid Rb is larger than that of solid Rb, which reflects the enhancement of thermal motion of ions upon melting. On the other hand, $\Delta E_{1/2}^{\text{ion}}(0)$ of liquid Rb is smaller than that of solid Rb, which causes the decrease in $\Delta E_{1/2}^{\text{calc}}(0)$ ($= \Delta E_{1/2}^{\text{ion}}(0) + \Delta E_{1/2}^{\text{ph}}(0)$). Because the decrease in $\Delta E_{1/2}^{\text{ion}}(0)$ originates from the structural difference between solid and liquid Rb, we can interpret that the effect of the ionic potential on the plasmon damping is suppressed accompanied by the vanishing of the crystalline structure.

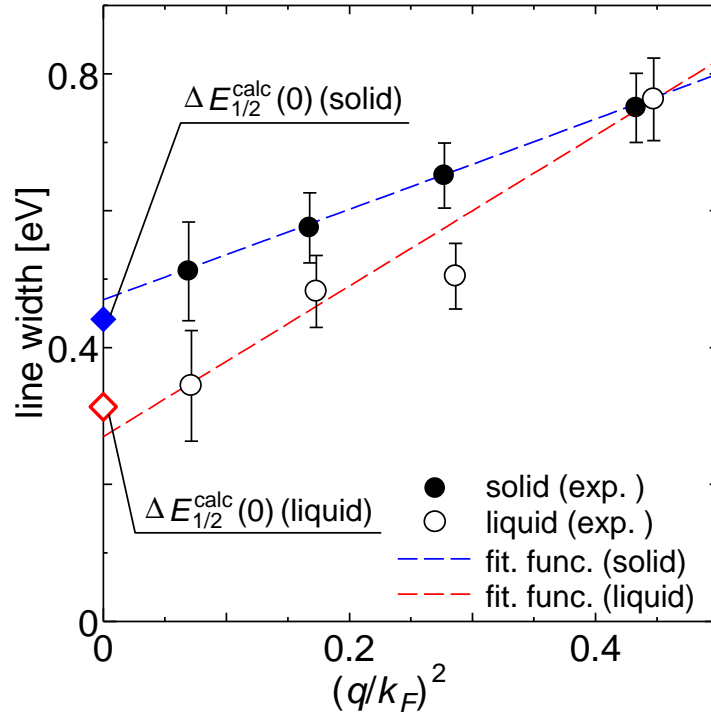


Figure 4.9: Plasmon line widths of solid and liquid Rb in small q region are plotted against $(q/k_F)^2$, where k_F is the Fermi wave number. Closed circles show the experimental data for solid Rb and open circles for liquid Rb. Diamonds indicate the calculation for the solid and the liquid state at $q = 0$. Dashed lines are the quadratic functions of q fitted to the experimental data.

Table 4.4: Experimental value of the line width at $q = 0$ ($\Delta E_{1/2}^{\text{exp}}(0)$) and calculated one ($\Delta E_{1/2}^{\text{calc}}(0)$), which is a sum of the ionic part ($\Delta E_{1/2}^{\text{ion}}(0)$) and the phonon part ($\Delta E_{1/2}^{\text{ph}}(0)$). All values are in eV.

	$\Delta E_{1/2}^{\text{exp}}(0)$	$\Delta E_{1/2}^{\text{calc}}(0)$	$\Delta E_{1/2}^{\text{ion}}(0)$	$\Delta E_{1/2}^{\text{ph}}(0)$
Solid	0.47 ± 0.07	0.44	0.42	0.022
Liquid	0.27 ± 0.13	0.31	0.27	0.043

4.3 Summary

We have performed IXS measurements for solid and liquid Rb, and determined the plasmon dispersion. Whereas the cusp-like shape of the dispersion curve is observed for the solid state, the plasmon energy of liquid Rb monotonically increases with q . With the aid of theoretical DOS of solid and liquid Rb, we have attributed this variation in the plasmon dispersion upon melting to the reduction of the band structure effect, and it has been suggested that the cusp-like shape of the dispersion curve in solid Rb originates from the interband transitions to the unoccupied d -states. We have also derived the q dependence of the line width, and found that the line width becomes narrower upon melting near $q = 0$. This narrowing is reproduced by the theoretical evaluation of the line widths in the solid and liquid states, from which we have interpreted that the influence of the ionic potential on the plasmon decay reduces accompanied by structural variation upon melting.

The observed variation in the plasmon dispersions of Rb upon melting suggests that the band structure effect, which is not considered in electron gas model, is less important in the liquid state than in the solid state. In addition, the line width of liquid Rb near $q = 0$ tends to be closer to the electron gas value than that of solid Rb. (The plasmon in the electron gas has infinite life time at $q=0$.) These observations suggest that the plasmon behaviors in Rb are better described with the electron gas model in the liquid state than in the solid state.

Chapter 5

Plasmons in Liquid Cs

We have performed IXS experiments for liquid Cs, to ascertain whether the variation in the unoccupied d -states upon melting is also reflected in the plasmon dispersion of Cs, as in the case of Rb. Because the unoccupied d -states in Cs largely change upon melting [14], comparison of the plasmon dispersion in solid Cs with that in liquid Cs will provide useful insight into the influence of the band structure effect on the negative dispersion of solid Cs, which was previously observed in EELS measurements [20].

In this chapter, the IXS spectra of liquid Cs [68] are presented. The plasmon dispersion relations and the line width are derived from these IXS spectra, and compared with those of solid Cs, obtained in previous EELS experiments [20]. The difference of the plasmon dispersions between solid and liquid Cs is discussed.

5.1 Results

Figure 5.1 shows the raw IXS spectra of liquid Cs. The scattering angles and the corresponding q where the IXS measurements were performed are shown in Table 5.1. The inelastic peak is observed at about ~ 13839 eV. The high intensity around 13837 eV is due to the quasielastic peak.

Table 5.1: The scattering angles and the corresponding momentum transfers q at which the measurements were performed.

2θ [°]	2.62	2.96	3.28	3.69	4.52
q [Å ⁻¹]	0.32	0.36	0.40	0.45	0.55

Figure 5.2 shows the IXS spectra of liquid Cs as a function of the energy transfer, $\hbar\omega$, normalized by the incident beam intensity. The energy transfer is obtained from the same procedure as described in section 4.1. The peak arising from plasmon is observed for each q at about $\hbar\omega \sim 2.7$ eV. The solid curves indicate the fitting functions. We used the same fitting function as in the case of Rb, that is, the sum of two Lorentzians convoluted with Gaussian. The FWHM of the Gaussian was set to the energy resolution 0.22 eV, which was derived from the FWHM of the quasielastic peak. It should be stressed that we can not see the negative dispersion in this q range, whereas the negative dispersion was observed in solid Cs for $q \leq 0.5$ Å⁻¹ in the EELS study [20].

Figure 5.3 (a) shows the plasmon dispersion of liquid Cs, determined by the fitting to the IXS spectra. In this figure, the dispersion of solid Cs taken from the EELS study [20] is also shown. While the plasmon disperses negatively in solid Cs for $0.10 \text{ \AA}^{-1} \leq q \leq 0.50 \text{ \AA}^{-1}$, the plasmon in liquid Cs tends to disperse positively for $0.32 \text{ \AA}^{-1} \leq q \leq 0.55 \text{ \AA}^{-1}$.

Figure 5.3 (b) shows the q dependence of the line width in liquid Cs. Here, the results of the EELS experiments [20] for solid Cs are also indicated. The data points of liquid Cs are located near those of solid Cs. According to the theoretical evaluation of the line width at $q = 0$ [51], which is described in Chapter 3, the line width of liquid Cs is narrower than that of solid Cs in the long-wavelength limit. However, our data in Fig. 5.3 (b) are so scattered that it is difficult to discuss the variation in the line width upon melting. Therefore, we focus on the discussion of the plasmon energy, hereafter.

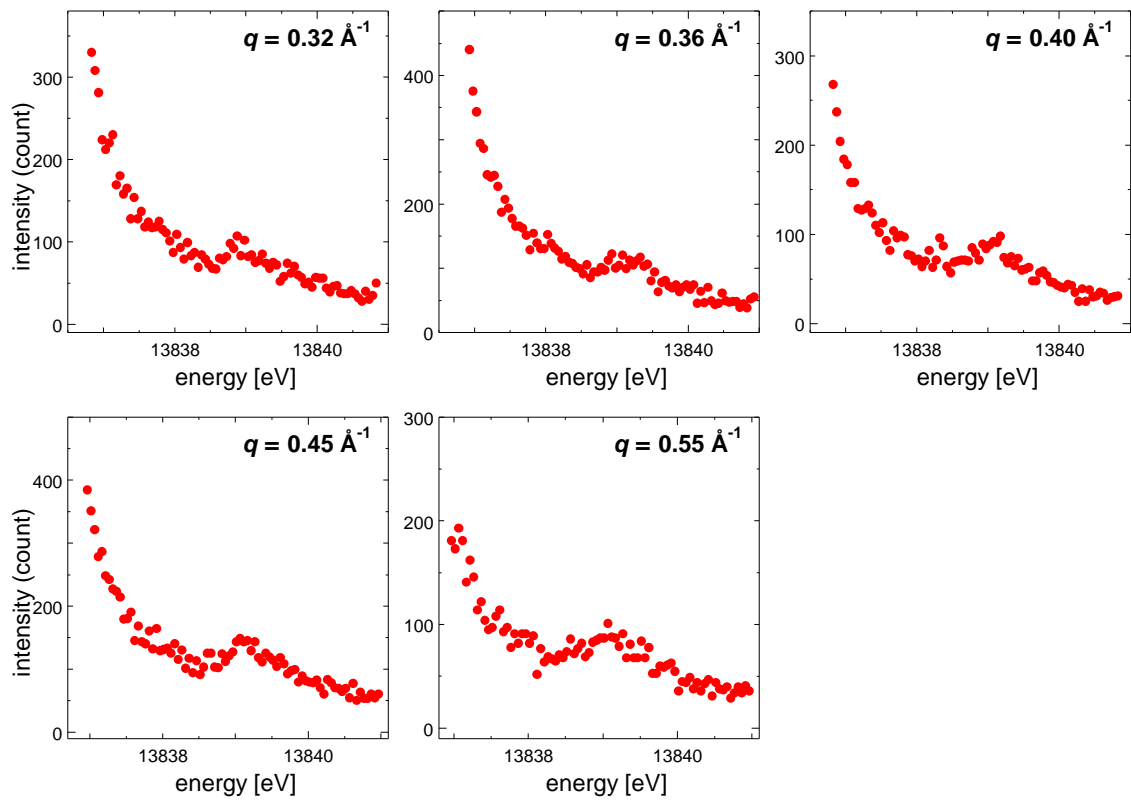


Figure 5.1: Raw IXS spectra of liquid Cs. The horizontal axes correspond to the energy of the scattered x-ray. The vertical axes are the total counts. The momentum transfers are denoted as q .

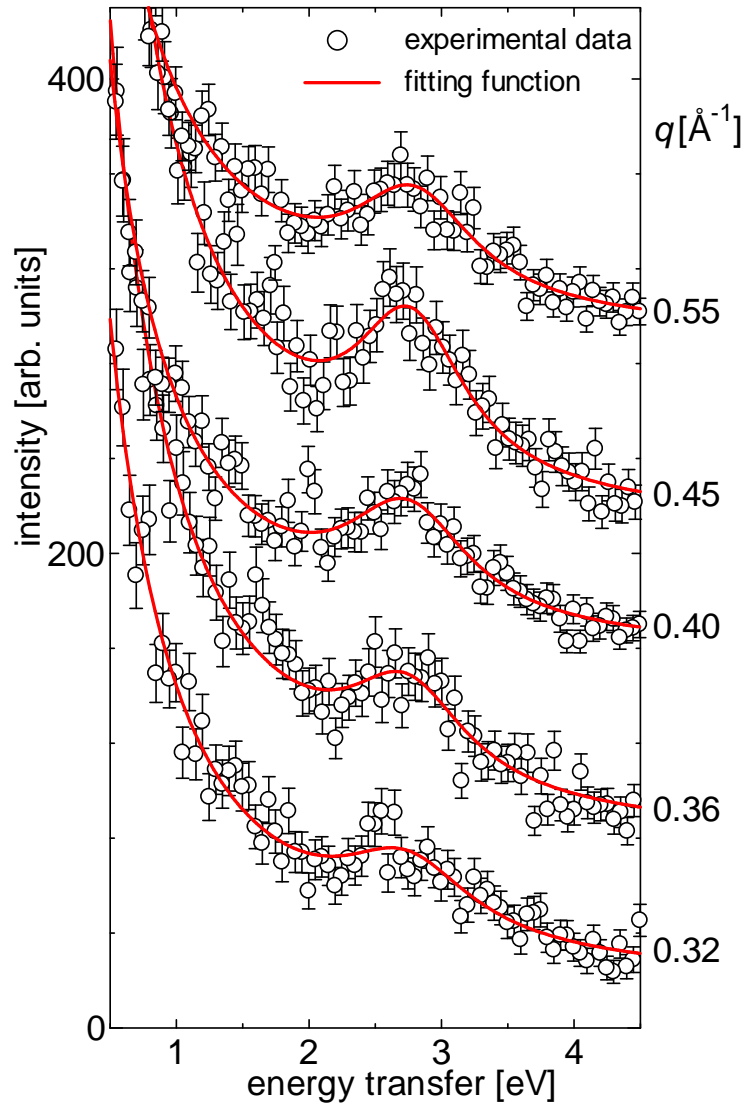


Figure 5.2: IXS spectra of liquid Cs normalized by the incident beam intensity. Values on the right side of the figure are the momentum transfers. Solid curves indicate the fitting functions.

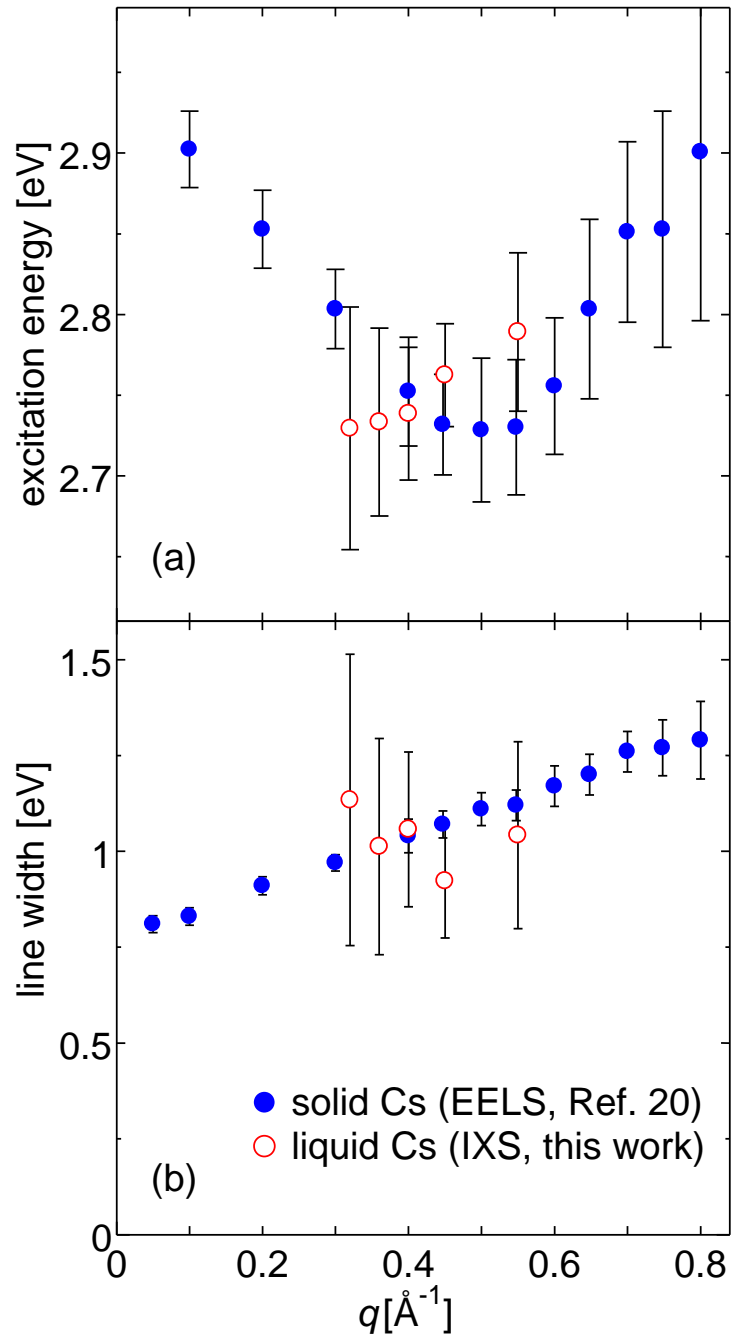


Figure 5.3: (a) Plasmon dispersion and (b) q dependence of the line width in liquid Cs and solid Cs. The experimental data of solid Cs were taken from the EELS experiment [20].

5.2 Discussion

As in the case of Rb, we discuss the unoccupied DOS of solid and liquid Cs in order to figure out how the band structure effect changes upon melting.

Figure 5.4 shows the DOS of solid and liquid Cs, which was calculated by Jank and Hafner [14]. The total DOS are indicated by solid curves and the d -state contributions are shown with dashed curves. The DOS of free electrons corresponding to the electron density of Cs is also shown for comparison. The shaded area indicates the energy range where the plasmons are observed in the IXS experiments.

As qualitatively discussed in section 4.2, interband transitions to the unoccupied states above plasmon energy have the effect of lowering the plasmon energy. The DOS of solid Cs is much larger than that of liquid Cs in the range of 3 - 4 eV, the energy range immediately above the shaded area (Fig. 5.4). Therefore, lowering of the plasmon energy due to interband transitions should be larger in the solid state than in the liquid state. Because the DOS in 3 - 4 eV is dominated by the d -states, such a lowering occurs for the q at which s - d transitions are allowed. Since s - d transitions are promoted as q increases, the plasmon energy of solid Cs should be more strongly lowered as q increases, which is consistent with the experimental observation that the plasmon energy of solid Cs becomes lower than that of liquid Cs for larger q (Fig. 5.3 (a)). Therefore, as in the case of Rb, the variation in the plasmon dispersion of Cs upon melting is attributable to the reduction of the band structure effect. Our interpretation is consistent with the theoretical work of Fleszar *et al.* [29], who showed that interband transitions to the d -states in DOS of solid Cs in 3 - 4 eV cause the lowering of the plasmon energy. The variation in the plasmon dispersion of Cs upon melting suggests that the band structure effect contributes to the negative dispersion in solid Cs.

Figure 5.5 shows plasmon dispersions of alkali metals normalized by the plasmon energy at $q = 0$, $\omega_p(0)$. The dispersion of liquid Cs obtained in this study is indicated by open squares. We evaluated $\omega_p(0)$ of liquid Cs to be 2.82 eV as follows. The $\omega_p(0)$ of solid Cs is estimated to be 2.95 eV, which is obtained by extrapolating the

EELS data with the quadratic function of q . The density of solid Cs is 1.99 g cm^{-3} , which is calculated from the lattice constant of Cs at 78 K, 6.05 \AA^{-1} [59]. The density of liquid Cs at 313 K is 1.82 g cm^{-3} [69]. From these values $\omega_p(0)$ of liquid Cs is calculated as $2.95 \times \sqrt{1.82/1.99} = 2.82 \text{ eV}$.

As mentioned in the previous section, the negative dispersion is observed in solid Cs (closed squares). This behavior strongly deviates from the prediction by the electron gas model, considering that the r_s value of Cs is less than 6. On the other hand, the dispersion of liquid Cs agrees better with that of the electron gas model than the dispersion of solid Cs, that is, the degree of the negative dispersion is smaller in liquid Cs than in solid Cs. The better agreement of the plasmon dispersion in the liquid state with the electron gas prediction than in the solid state is observed also for Rb. The plasmon energy tends to disperse positively in liquid Rb (open circles), whereas the dispersion in solid Rb (closed circles) shows cusp-like shape, as mentioned in the previous chapter. Therefore, the tendency that the plasmon dispersion approaches to the electron gas prediction upon melting is the common feature in heavy alkali metals. This tendency is consistent with our interpretation that the band structure effect reduces upon melting in Rb and Cs.

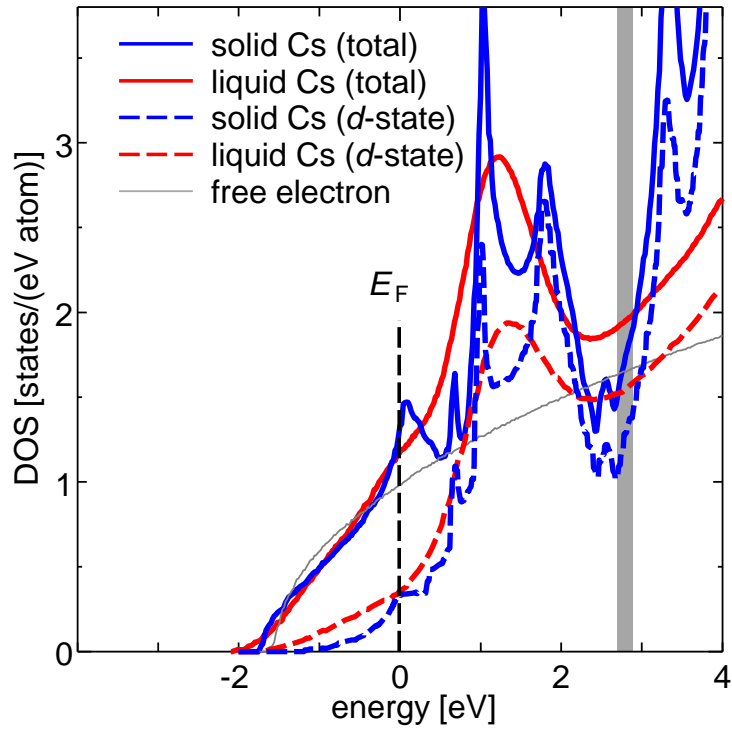


Figure 5.4: Theoretical electronic density of states (DOS) of solid and liquid (303 K) Cs, which was calculated by Jank and Hafner [14]. The thick solid curves and dashed curves show the total and partial (*d*-state) DOS, respectively. For comparison, the DOS of free electrons is indicated with thin solid curve. The shaded area shows the energy range where the plasmon is observed in this study.

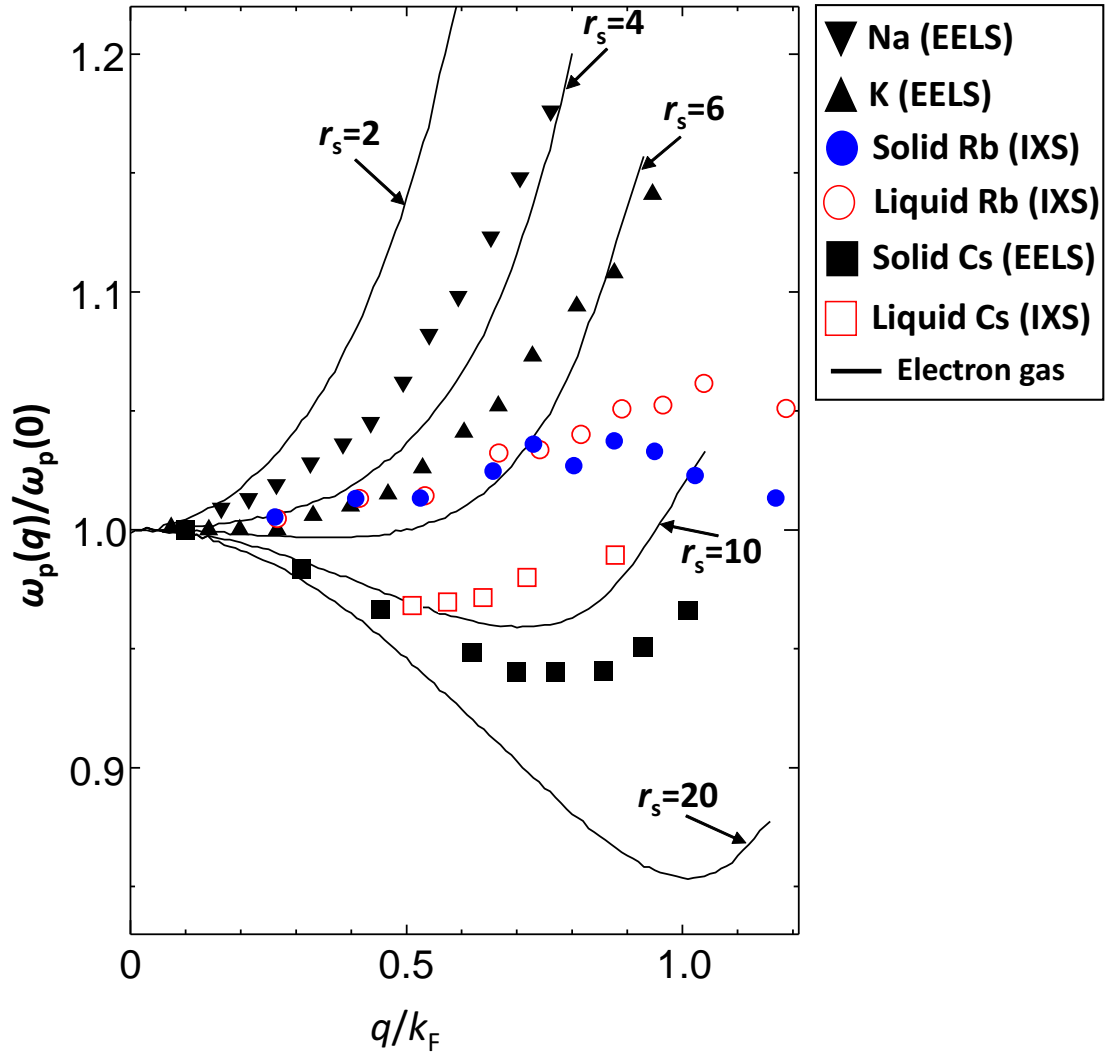


Figure 5.5: Plasmon dispersions of alkali metals normalized by the plasmon energy at $q = 0$. The plasmon dispersions of solid and liquid Rb, and of liquid Cs, which are obtained in this work, are indicated by closed circles, open circles, and open squares, respectively. The experimental results for solid Na, K, and Cs, determined by the EELS measurements [20], are indicated by inverted triangles, triangles, and closed squares, respectively. Solid curves are the theoretical plasmon dispersions of the interacting electron gas for various r_s , calculated by Singwi *et al.* [21].

5.3 Summary

We have carried out IXS measurements for liquid Cs, and determined the plasmon dispersion. The plasmon energy of liquid Cs tends to disperse positively within $0.32 \text{ \AA}^{-1} \leq q \leq 0.55 \text{ \AA}^{-1}$, whereas the plasmon energy of solid Cs disperses negatively within the corresponding q range, according to the previous EELS study [20]. From the comparison of the unoccupied DOS of solid Cs with that of liquid Cs, we have attributed the variation in the plasmon dispersion in Cs to the reduction of the band structure effect upon melting. In addition, it is indicated that the band structure effect contributes to the negative dispersion in solid Cs, which has been pointed out theoretically so far.

The observed variation in the plasmon dispersion upon melting suggests that plasmon behaviors in the liquid state are more suitably described with the electron gas model than those in the solid state not only in the case of Rb but also in the case of Cs.

Chapter 6

Conclusion

In this work, plasmon behaviors in liquid alkali metals near the melting point have been investigated. We have performed IXS experiments for solid and liquid Rb, and for liquid Cs. The plasmon dispersion relations and the line width have been derived from the IXS spectra, and the variation in these properties upon melting have been discussed. We have also derived a formula for evaluating the plasmon line width of liquid metals at the long-wavelength limit.

In Chapter 3, a formula for evaluating the plasmon line width of liquid metals at $q = 0$ has been derived. We have applied this formula to liquid alkali metals, and found that the line width becomes narrower upon melting. This narrowing quantitatively explains our experimental results for solid and liquid Rb, and qualitatively accounts for the tendency that the line width of Li becomes smaller upon melting, which was observed in the previous IXS study [16].

In Chapter 4, the IXS spectra of solid and liquid Rb have been presented, and the plasmon dispersion relations have been derived. We have found that the plasmon energy of liquid Rb monotonically increases with q , whereas the cusp-like dispersion curve has been observed for solid Rb. We have compared the DOS of liquid Rb with that of solid Rb, from which we have interpreted that the variation in the plasmon dispersion upon melting is attributable to the reduction of the band structure effect. Therefore, it has been suggested that the cusp-like dispersion in solid Rb originates from the band structure effect. The plasmon line width has also been derived from

the IXS spectra. We have found that the line width of liquid Rb is narrower than that of solid Rb near $q = 0$. Based on the calculation of the line width for both solid and liquid Rb, which is described in Chapter 3, we have interpreted that the narrowing of the line width originates from the reduction in the effect of ionic potential accompanied by the structural variation upon melting.

In Chapter 5, the IXS spectra of liquid Cs have been presented. We have derived the plasmon dispersion, and compared it with the plasmon dispersion of solid Cs, which was determined in the previous EELS study [20]. We have revealed that the plasmon of liquid Cs tends to disperse positively for $0.32 \text{ \AA}^{-1} \leq q \leq 0.55 \text{ \AA}^{-1}$, while plasmon of solid Cs shows negative dispersion for the corresponding q , according to the EELS measurements. As in the case of Rb, we have interpreted that this variation in the plasmon dispersion originates from the reduction of the band structure effect, with the aid of theoretical DOS of solid and liquid Cs. Thus, it has been experimentally indicated that the band structure effect contributes to the negative dispersion in solid Cs.

The narrowing of the line width and the observed variation in the plasmon energy indicate that the effect of ionic potential on plasmon, which is not included in electron gas model, reduces upon melting in the heavy alkali metals. Therefore, it is suggested that the behaviors of valence electrons, at least the plasmon behaviors, in liquid Rb and Cs are more suitably described with the electron gas model than those in solid Rb and Cs.

Our IXS measurements for heavy alkali metals provide valuable insight into the anomalous plasmon dispersions in solid Rb and Cs observed in EELS study, which have been a subject of controversy for a long time but have not been investigated experimentally. This insight will be useful to refine the treatment of the XC effect and the band structure effect in many-body systems. The formulation for the plasmon line width in liquid metals gives fundamental understanding of how the ionic structure and the electronic states are related in liquid metals. This insight will be required to investigate the electronic states in fluid Rb and Cs at high temperature and high pressure, and also will lead us to clarify the electronic properties in

other disordered systems, such as amorphous solids, metallic glasses, or warm dense matter.

Appendix

Preparations for IXS Experiments up to the Liquid-Vapor Critical Point

For investigating the electronic excitations in alkali metals using IXS up to the critical point, the sapphire cell [47] is not usable because of the high reactivity of the hot alkali metals to sapphire. Refractory metals, such as Molybdenum, Tungsten, or Rhenium alloys, are suitable to hold the alkali metals near the critical point [1]. So far, such metals have been used in the neutron diffraction experiments [57], x-ray diffraction experiments [70, 12], or the measurements of the equation of state and transport properties [71] for alkali metals near the critical point. However, a sample cell to carry out IXS experiments for alkali metals in extreme conditions has not been developed until now. Because the signal of IXS is much weaker than in the case of the diffraction measurements, thinner x-ray windows are required to obtain enough statistical accuracy for reliable analysis of IXS spectra under high temperatures and pressures up to the critical regions.

This appendix describes a newly developed metallic cell made of Niobium (Nb), which is designed to measure IXS from liquid alkali metals in extreme conditions. In addition, a high-pressure vessel which can pressurize the sample with He gas is described. Finally, IXS spectra up to 1273 K at 5 MPa are presented.

A1. Niobium Cell

Figure 1 (a) shows the construction of the Nb cell, and Fig. 1 (b) shows the enlargement of the sample space (the area enclosed with the circle). All components are made of Nb. The cell consists of (1) an outer pipe (6.0 mm external diameter, 4.1 mm internal diameter), (2) an inner pipe A (4.0 mm external diameter, 1.0 mm internal diameter near the sample space), (3) an inner pipe B (4.0 mm external diameter, 1.0 mm internal diameter), (4) a reservoir, (5) thin foils (x-ray window, 15 μm thick), (6) a ‘C’-shape ring, (7) ‘O’-shape rings. The thickness of the x-ray window (15 μm) is much smaller than that in the previous work (40 μm) [70]. Figure 1 (c) shows the ‘C’-shape and ‘O’-shape ring, which determine the thickness of the sample space. The thicknesses of these rings are 100 μm , and thus the thickness of the sample space is 300 μm , which is suitable to the IXS measurements for Rb at 13.8 keV as mentioned in Chapter 2. In addition ‘O’-shape rings are necessary to prevent the thin foils from bending, especially in the process of joining the thin foils to the inner pipes as described below.

All parts, except for ‘C’-shape ring, are joined together by electron beam welding (EBW). EBW technique can be applied to metals which have high melting point. Furthermore, the position of the beam spot can be controlled with high precision. As shown below, in the cell assembling process, precise control of the welded part is required. Therefore, to weld the parts of the cell made of Nb (melting point is ~ 2750 K), EBW technique is crucially important.

Figure 2 (a) illustrates the procedure for welding the thin foil to the inner pipes A, B. As shown in the right side of this figure, we use a stainless holder, which can fix the thin foil attached on the inner pipe. The ‘O’-shape ring is put on the thin foil to avoid the bending of the thin foil, and to ensure the contact between the thin foil and the inner pipe. In addition, a back-up spring is set as indicated in the figure, so that these parts tightly contact with each other. Then, electron beam is irradiated on the ‘O’-shape ring, and moves in a manner to draw a circle. The beam penetrates into the inner pipe, and consequently these three parts (‘O’-shape ring,

thin foil, inner pipe) are welded together. Figure 3 (a) shows a picture of the welded parts (the top view of the right figure in Fig. 2 (a) after the welding). We can see the clear weld bead on the ‘O’-shape ring.

After the procedure described in Figure 2 (a), the inner pipes A, B, the outer pipe, and the reservoir are assembled together, as shown in Fig. 2 (b). The inner pipe B is first inserted into the outer pipe and welded together. Then, the ‘C’-shape ring and the inner pipe A are inserted into the outer pipe, and the inner pipe A is welded to the outer pipe. Finally, the reservoir is welded to the outer pipe. The EBW is again used for welding these parts.

Following the above procedure, we have completed the fabrication of the cell. Figure 3 (b) shows the picture of the Nb cell after the assembling. The sealing test of the cell was done as described in Chapter 2, and we confirmed that there was no leakage of He gas from the cell.

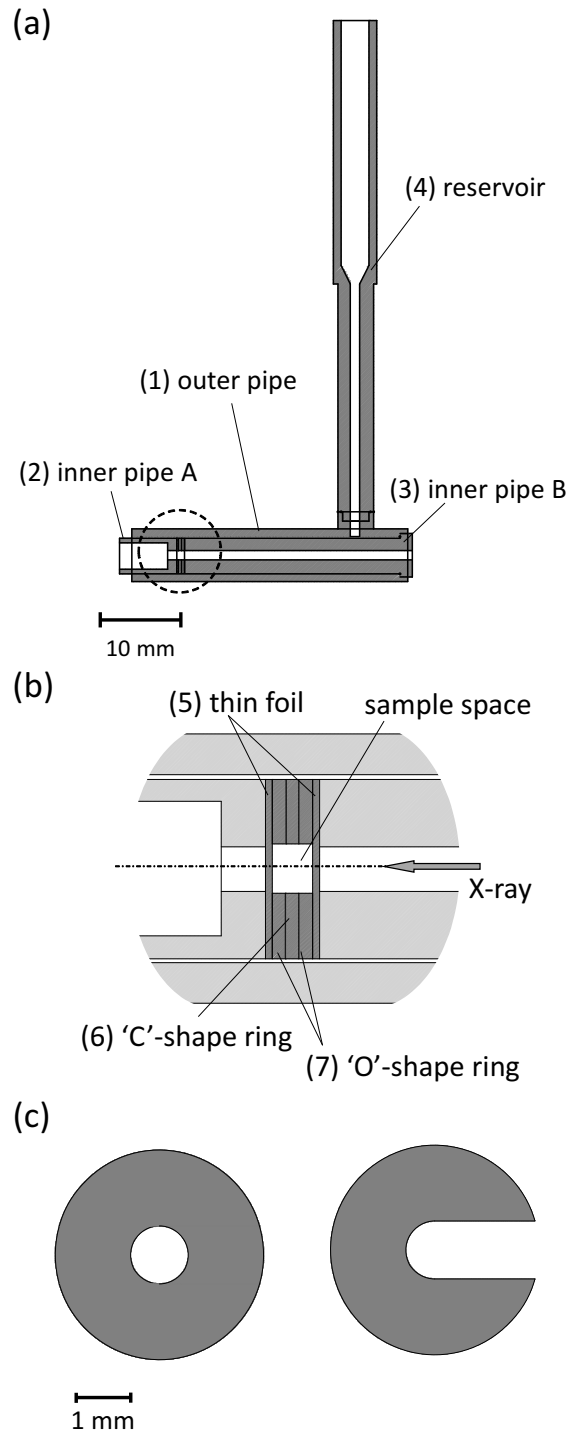


Figure 1: (a) Construction of the Nb cell. (b) Enlargement of the area enclosed by circle in (a). (c) A 'C'-shape ring and a 'O'-shape ring.

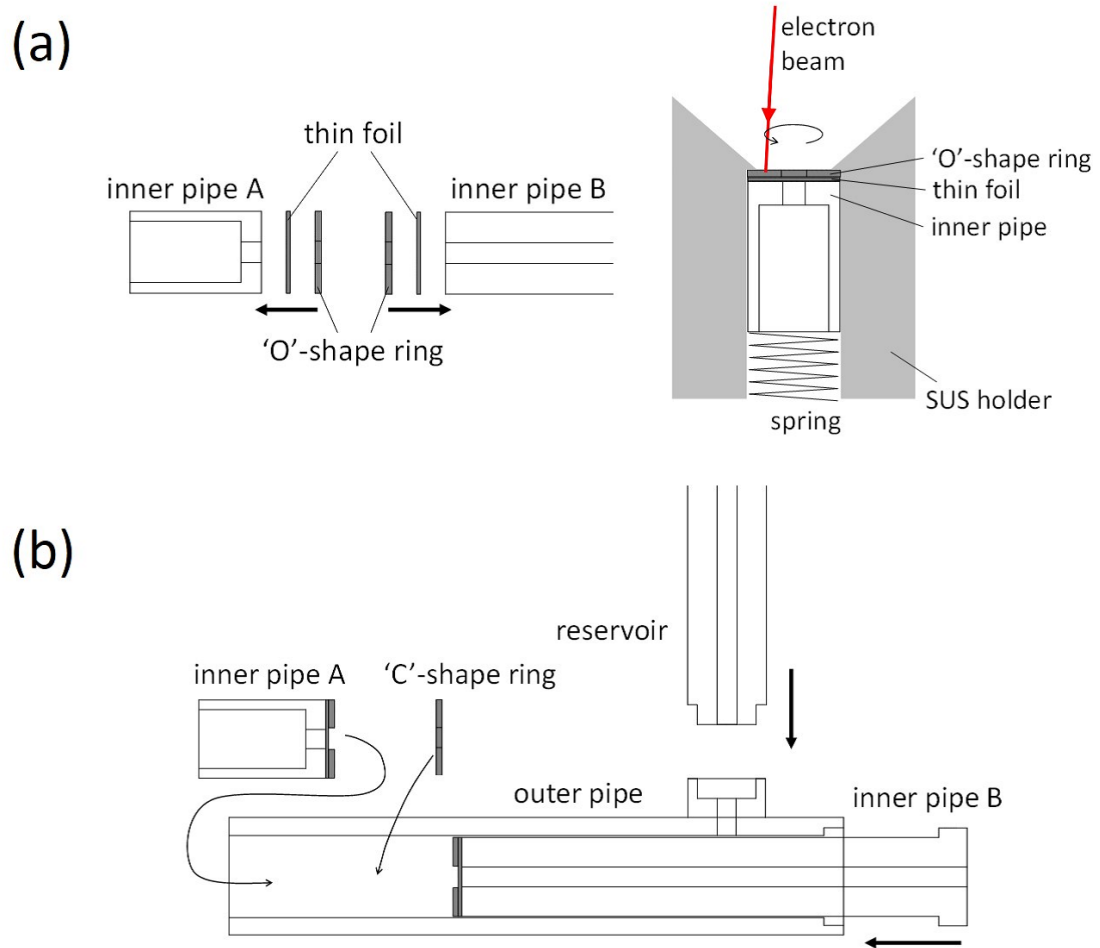


Figure 2: Assembling process of the Nb cell. (a) Procedure of welding the thin foil and the inner pipe. (b) Procedure of assembling the inner pipe A, B, outer pipe and reservoir. The parts are joined with electron beam welding technique.

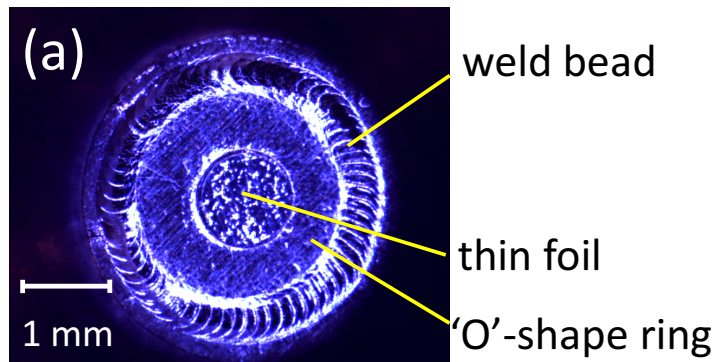


Figure 3: (a) Picture of the weld bead on the 'O'-shape ring. (Top view of the right figure in Fig. 2 (a) after the welding.) (b) Picture of the fabricated Nb cell.

A2. High Pressure Vessel

To achieve high temperature and high pressure conditions, we have developed an internally heated high-pressure vessel (HPV). The maximum pressure and temperature that can be used in this HPV are 25 MPa and 1700 °C.

Figure 4 shows a side view of the HPV. The HPV consists of a main cylinder, an upper flange, and a lower flange. The HPV is pressurized by He gas, which is introduced through a path in the upper flange. Beryllium (Be) disks (10 mm thickness) are used for the x-ray windows. The electrodes and the thermocouples are introduced into the inside of the HPV through the lower flange, where Bridgeman-type high-pressure seals are used (described later). To prevent overheating of the cylinder and the flanges during the high-temperature experiments, cooling water jacket is placed around the outside of the HPV.

Figure 5 shows the upper view of the HPV. The Be windows are placed so that the scattered x-rays with the scattering angle below $\sim 20^\circ$ can be measured.

Figure 6 shows the construction of the Bridgeman-type high-pressure seals for the electrodes and the thermocouples [72, 47]. The seal is made of Teflon, which is put between bakelites. The edge of the Teflon is sandwiched with the brass delta rings. The uppermost screw compresses these parts through the stainless parts and the Teflon is squashed, so that the sealing becomes tight. The electrical isolation of the electrodes is made using glass tubes. For the isolation of thermocouples, Teflon tubes and alumina tubes are used.

Figure 7 shows the Nb cell inserted into the furnace in the HPV. As in the case of the sapphire cell, described in Chapter 2, the Nb cell is inserted in the Mo tube, to which the heater (main heater) and the thermocouples are fixed. As a heating element a Tungsten (W) wire is used. For monitoring temperature, Tungsten-Rhenium (W-Re) thermocouples are used. Alumina tubes are used for electrical insulation. Additional W-heater is attached around the reservoir of the cell (subsidiary heater). If the sample melts only near the sample space, leaving the rest of the sample in the solid state, the thin x-ray windows (15 μm thick) will be damaged owing to the

expansion of the sample upon melting. To avoid this damage, the sample in the reservoir is heated with the subsidiary heater before switching on the main heater. In addition, a copper cooling stage is attached around the reservoir, in order to avoid the exhaustion of the sample owing to the evaporation at high temperatures.

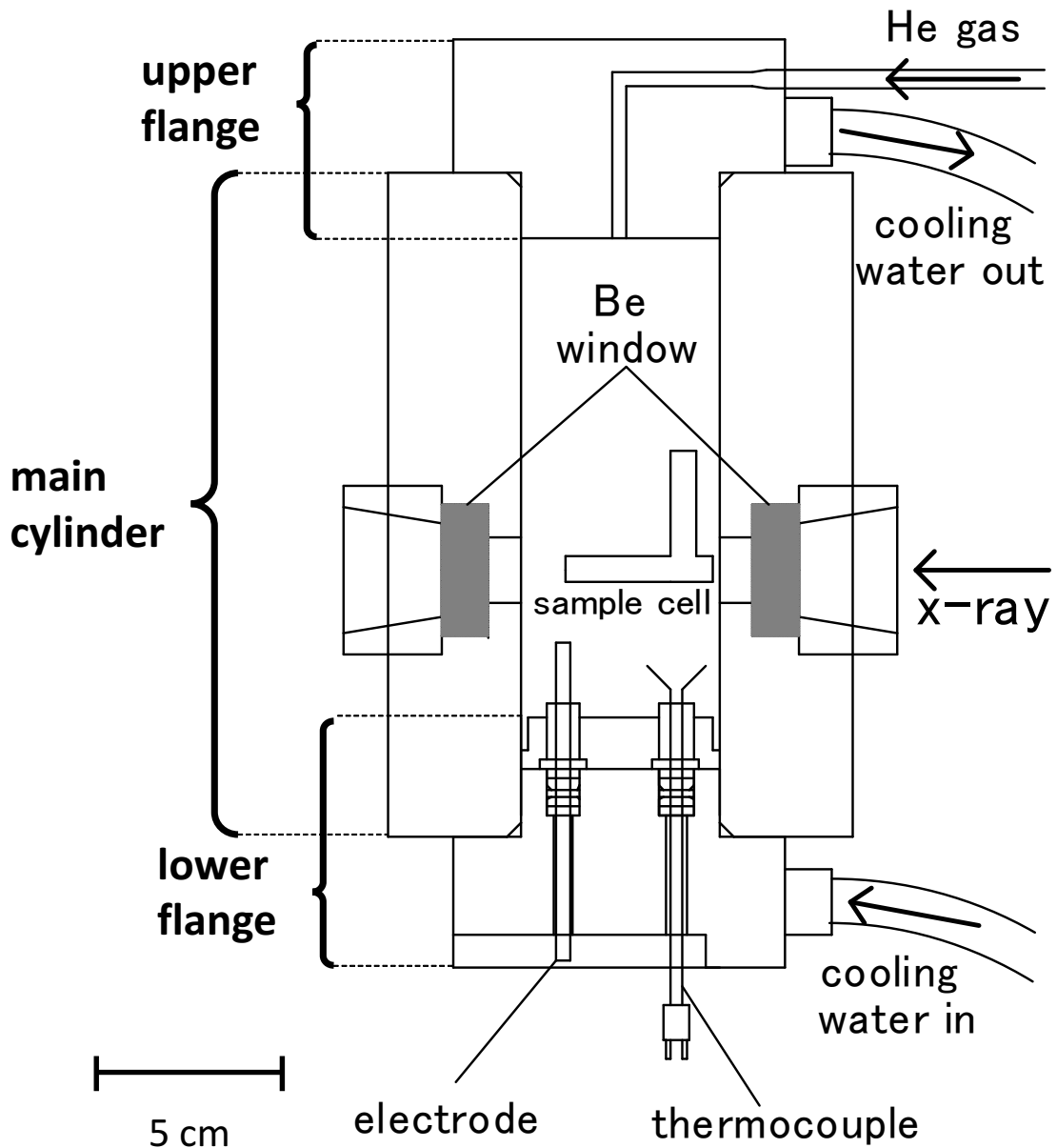


Figure 4: Side view of the high-pressure vessel.

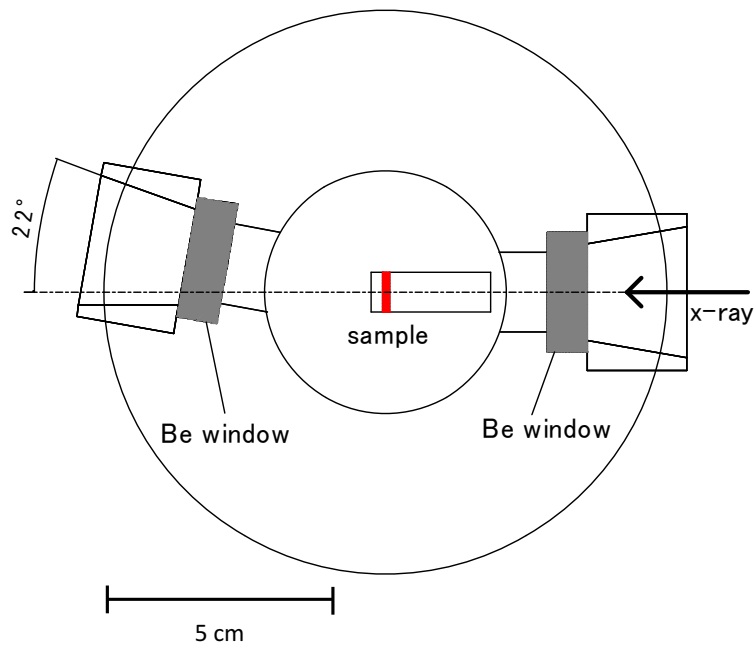


Figure 5: Top view of the high-pressure vessel.

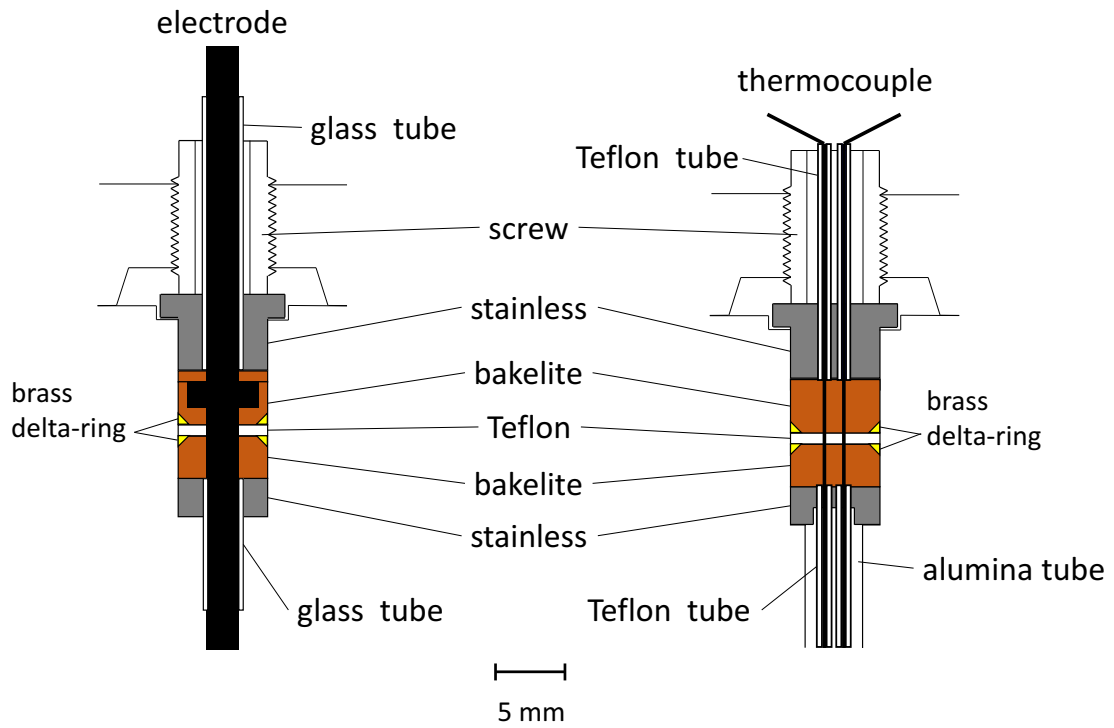


Figure 6: Bridgeman-type high-pressure seal for electrodes (left) and thermocouples (right).

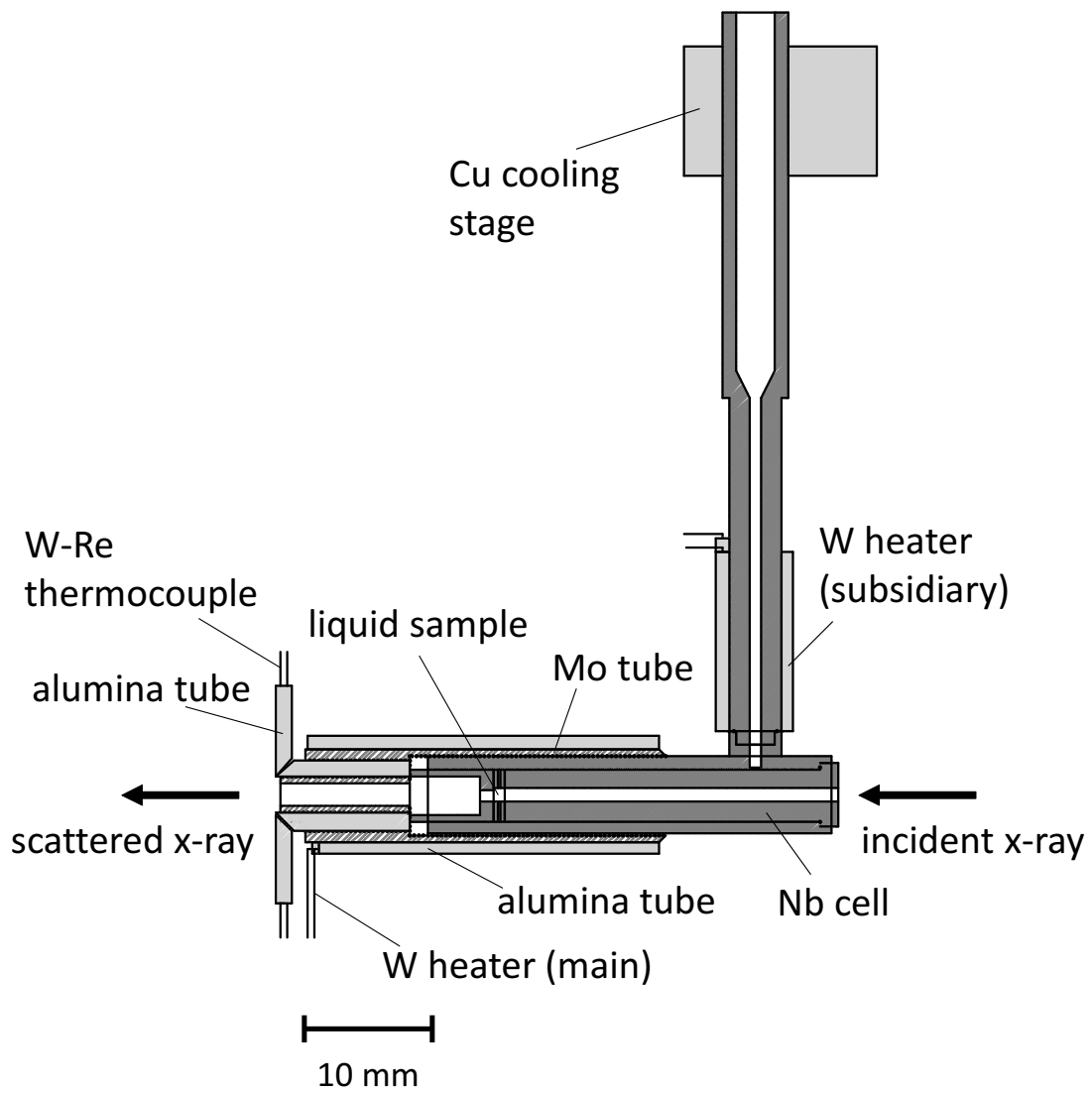


Figure 7: Furnace in the HPV, into which the Nb cell is inserted.

A3. IXS spectrum for liquid Rb up to 1273 K at 5 MPa

We have performed IXS experiments for liquid Rb at high temperatures under the gas compression, using the newly developed Nb cell and high-pressure vessel. The sample was introduced into the cell as described in Chapter 2. The measurements were carried out on the Taiwan inelastic x-ray scattering beamline BL12XU [49], as in the case of the measurements near the melting point (Chapter 2). We have succeeded in obtaining IXS spectrum at 1273 K and 5 MPa and confirmed that the Nb cell is applicable to the IXS measurements for liquid Rb at high temperature and high pressure.

The IXS spectra were obtained at temperatures 573 K, 773 K, 1073 K, and 1273 K. So far, IXS experiment to observe phonons [73] has been performed for Na up to 1173 K using the sapphire cell, without chemical corrosion. Considering this, the IXS experiments at 1273 K were performed with the Nb cell, and those at 573 K, 773 K, 1073 K were done using the sapphire cell. We also performed IXS measurements at 573 K using the Nb cell, to confirm the reproducibility of the IXS spectrum. All measurements were performed at pressure of 5 MPa, using the HPV. The pressure was monitored with a Heise gauge.

Figure 8 compares the IXS spectrum of liquid Rb in the sapphire cell with that in the Nb cell, at 573 K and 5 MPa, and at momentum transfer $q = 0.70 \text{ \AA}^{-1}$. We can see that the spectrum obtained with the Nb cell is in good agreement with that obtained with the sapphire cell. The data of liquid Rb in the Nb cell are more scattered than in the case of the sapphire cell, because the measurement time is shorter than in the case of sapphire cell. For the measurement using Nb cell, the measurement time was ~ 1 hour, while in the case of the sapphire cell the measurement time was ~ 8 hours.

Figure 9 shows the IXS spectra of liquid Rb at $q = 0.70 \text{ \AA}^{-1}$, up to 1273 K at 5 MPa. The measurements took about 8 hours for each conditions. The figure also shows the spectrum at 333 K and 0.1 MPa, which is presented in Chapter 4. We can see that the inelastic peak position shifts to lower energy region as the

temperature increases, which is qualitatively consistent with the decrease in the density with increasing temperature. At 1273 K, the plasmon peak is not clearly observed. This is probably because the inelastic peak is merged into the quasielastic peak. In addition to the lowering of the plasmon energy with increasing temperature, the intensity of the quasielastic peak becomes larger as the temperature becomes higher, which makes it difficult to separate the inelastic peak from the quasielastic peak. This enhancement of the quasielastic contribution can be understood from the diffraction measurements for fluid Rb [57, 12], where the structure factor $S(q)$ in low q region (below $\sim 1 \text{ \AA}^{-1}$) increases with increasing temperature (decreasing density). To clearly observe plasmons beyond 1273 K, higher energy resolution should be required.

Although improvement of the energy resolution should be necessary to separate the inelastic peak from the quasielastic peak at 1273 K, our results demonstrate that the newly developed Nb cell can be applied to the IXS experiments for observation of electronic excitations in alkali metals under high temperatures and high pressures.

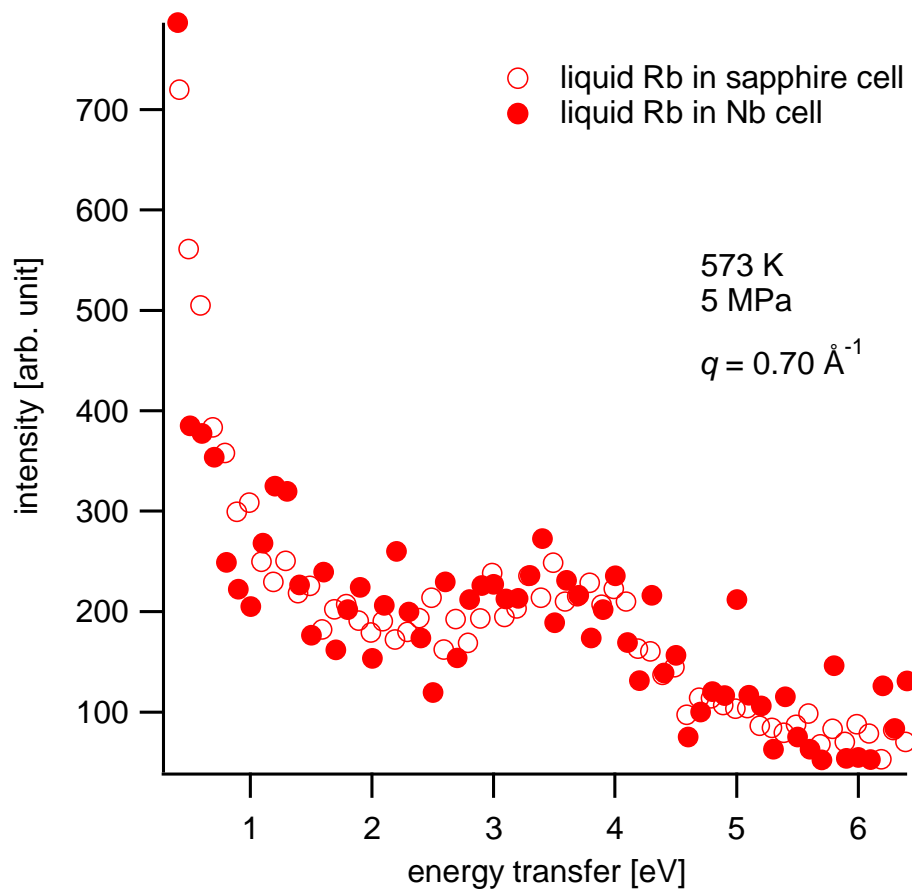


Figure 8: IXS spectra of liquid Rb in the sapphire cell (open circle) and in the Nb cell (closed circle) at $q = 0.70 \text{ \AA}^{-1}$. Temperature and pressure are 573 K and 5 MPa, respectively.

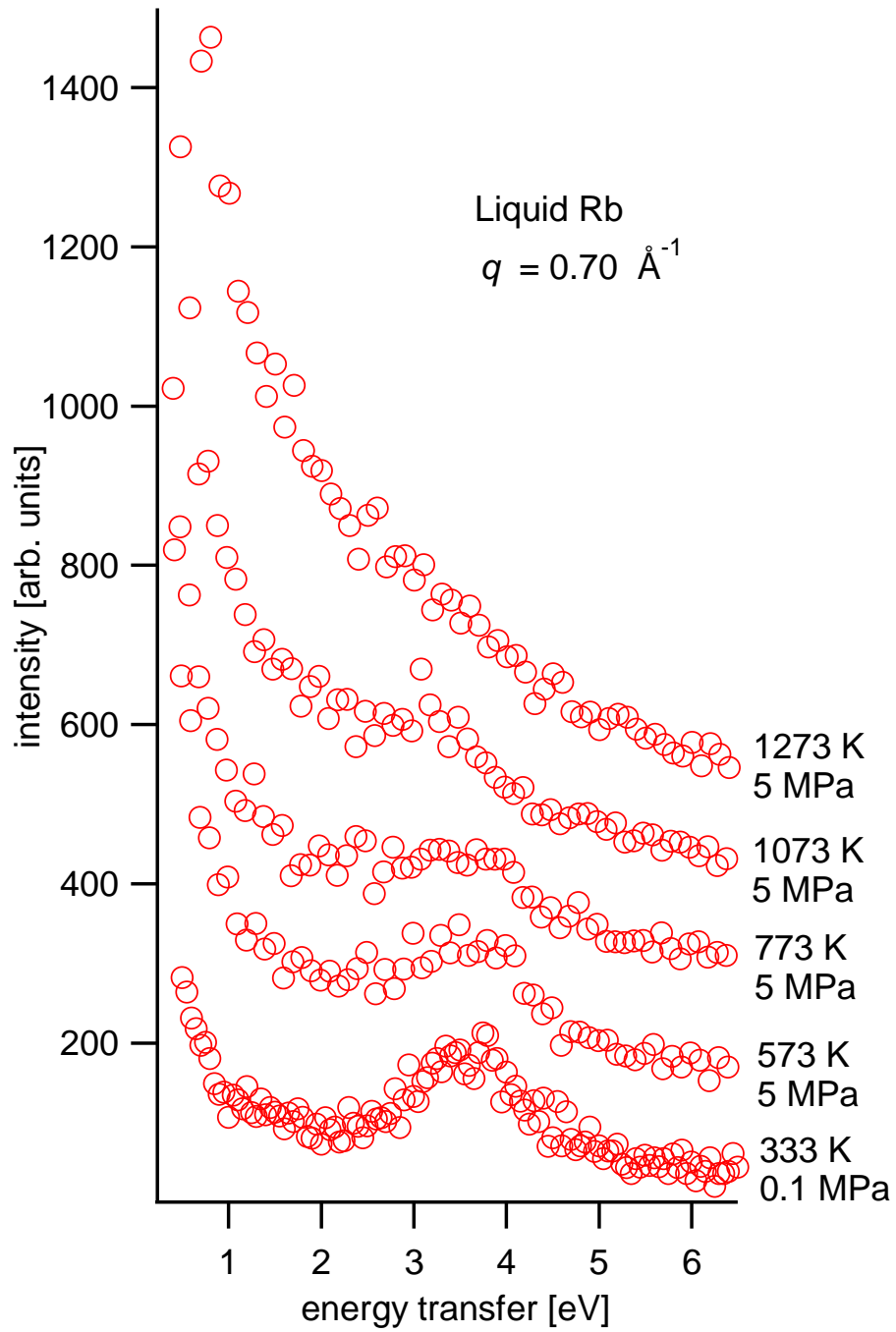


Figure 9: IXS spectra of liquid Rb up to 1273 K at 5 MPa. The momentum transfer is 0.70 \AA^{-1} . The IXS spectrum of liquid Rb at 333 K in the ambient pressure, which is taken from the data presented in Chapter 4, is also shown.

Acknowledgement

I would like to express my deepest gratitude to my supervisor Prof. Kazuhiro Matsuda, who led me to the fields of fluid metals and synchrotron radiation. He continuously supported me for planning and performing experiments. In addition, he advised me on how to write articles, and how to make presentations. Thanks to his instruction, I could learn various things required for the researchers.

I am deeply grateful to Prof. Makoto Yao, who gave me insightful suggestions for experimental results. Without his suggestion, Chapter 3 would not have materialized. He also provided useful comments for the articles and this thesis.

I would like to show my great appreciation to Dr. Nozomu Hiraoka, who have adjusted the alignment of the optical components in the beamline BL12XU at SPring-8 for the inelastic x-ray (IXS) scattering measurements. He has been always tolerant and supportive, although the experiments were demanding. He also gave me useful comments for analyzing the data.

I would like to thank Prof. Masanori Inui and Prof. Yukio Kajihara, who supported preparations for the experiment and IXS measurements at SPring-8. In particular, they gave me practical comments on how to make the sapphire cell.

I am grateful to Mr. J. Nakamura, T. Nagao, T. Fukumaru, Y. Ishiguro, T. Miyatake, and T. Hagiya, with whom I studied liquid metals. Their generous supports were invaluable. I wish to thank all the members of the Yao laboratory, Prof. K. Nagaya, and T. Nishiyama. I owe an important debt to Prof. Ohmura, who gave me warm encouragement. Discussions with him have been very interesting and constructive. I also thank Prof. A. N. Sobolev for providing the data of the DOS for

liquid Rb.

I want to thank Mr. T. Wakita, and K. Kitamura, who provided us the technical supports for fabricating the Niobium cell.

I am profoundly grateful to Mr. and Mrs. Fukumaru for their financial support. This work was supported by Grant-in-Aid for Scientific Research Fund, Toray Science Foundation, and the Global COE Program “The Next Generation of Physics, Spun from Universality and Emergence” from the Ministry of Education, Culture, Sports, Science and Technology of Japan. The synchrotron radiation experiments were performed at SPring-8 with the approval of Japan Synchrotron Radiation Research Institute (No. 2010B4260, No. 2011B4257, No. 2012B4261, No.2013A4259, 2014A4265, and 2014B4254) and the National Synchrotron Radiation Research Center (2010_2_009, 2012_3_034, 2013_2_074, 2014_2_073, and 2014_3_052).

Finally, I would like to thank my friends and family for their moral support.

References

- [1] F. Hensel, W. W. Warren, Jr., *Fluid Metals* (Princeton University Press, New Jersey, 1999).
- [2] J. M. Ziman, *Phil. Mag.* **6**, 1013 (1961).
- [3] N. E. Cusack, *The Physics of Structurally Disordered Matter* (University of Sussex Press, Philadelphia, 1987).
- [4] G. Franz, W. Freyland, and F. Hensel, *J. Phys. Colloque* **C8** 70 (1980).
- [5] R. Winter, F. Hensel, T. Bodensteiner, and W. Gläser, *Ber. Bunsenges. Phys. Chem.* **91**, 1327 (1987)
- [6] D. J. Fonzalez, D. A. NG, and m. Silbert, *J. Non-Cryst. Solids* **117** 469 (1990)
- [7] W. Freyland, *Phys. Rev. B* **20**, 5104 (1979).
- [8] W. Freyland, *J. Phys. (Paris), Colloq.* **41**, 74 (1980).
- [9] W. W. Warren, G. F. Brennert, and U. El-Hanany, *Phys. Rev. B* **39**, 4038 (1989).
- [10] B. Knuth, F. Hensel, and W. W. Warren Jr, *J. Phys.: Condens. Matter* **9** 2693 (1997).
- [11] S. Jüngst, B. Knuth, and F. Hensel, *Phys. Rev. Lett.* **55**, 2160 (1985).
- [12] K. Matsuda, K. Tamura, and M. Inui, *Phys. Rev. Lett.* **98**, 096401 (2007).
- [13] W. Jank, and J. Hafner, *J. Phys.: Condens. Matter* **2**, 5065 (1990).

- [14] W. Jank and J. Hafner, *J. Phys.: Condens. Matter* **3**, 6947(1991).
- [15] S. Krishnan, and P. C. Nordine, *Phys. Rev. B* **47**, 11780 (1993).
- [16] J. P. Hill, C. C. Kao, W. A. C. Caliebe, D. Gibbs, B. Hastings, *Phys. Rev. Lett.* **77**, 3665 (1996).
- [17] D. Pines, *Elementary Excitations in Solids* ((Benjamin, New York, 1964).
- [18] G. F. Giuliani, G. Vignale, *Quantum Theory of the Electron Liquid* (Cambridge University Press, New York, 2005).
- [19] M. Hasegawa, and M. Watabe, *J. Phys. Soc. Jpn.* **27**, 1393 (1969).
- [20] A. vom Felde, J. Sprösser-Prou, and J. Fink, *Phys. Rev. B* **40**, 10181 (1989).
- [21] K. S. Singwi, M. P. Tosi, R. H. Land, and A. Sjölander, *Phys. Rev.* **176**, 589 (1968).
- [22] Ll. Serra, F. Garcias, M. Barranco, N. Barberán, and J. Navarro, *Phys. Rev. B* **44**, 1492 (1991).
- [23] G. Kalman, K. Kempa, and M. Minella, *Phys. Rev. B* **43** 14238 (1991).
- [24] M. Taut, and K. Sturm, *Solid Commun.* **82**, 295 (1992).
- [25] M. Taut, *J. Phys.: Condens. Matter* **4**, 9595 (1992).
- [26] E. Lipparini, S. Stringari, and K. Takayanagi *J. Phys. Condens. Matter* **6**, 2025 (1994).
- [27] H. M. Böhm, S. Conti, and M. P. Tosi *J. Phys.: Condens. Matter* **8** 781 (1996).
- [28] F. Aryasetiawan and K. Karlsson, *Phys. Rev. Lett.* **73**, 1679 (1994).
- [29] A. Fleszar, R. Stumpf, and A. Eguiluz, *Phys. Rev. B* **55**, 2068 (1997).
- [30] M. Hasegawa, *J. Phys. Soc. Jpn.* **31**, 649 (1971).
- [31] K. Sturm, and L. E. Oliveira, *Phys. Rev. B* **24**, 3054 (1981).

- [32] C. Sternemann, A. Kaprolat, W. Schülke, Phys. Rev. B **57**, 622 (1998)
- [33] C. A. Burns, P. Abbamonte, E. D. Isaacs, and P. M. Platzman, Phys. Rev. Lett. **83**, 2390 (1999).
- [34] H. Hayashi, Y. Udagawa, C.-C. Kao, J.-P. Rueff, and F. Sette, J. Electron Spectrosc. Relat. Phenom. **120**, 113 (2001).
- [35] C. A. Burns, P. Giura, A. Said, A. Shukla, G. Vankó, M. Tuel-Benckendorf, E. D. Isaacs, P. M. Platzman Phys. Rev. Lett. **89**, 236404 (2002).
- [36] X. Wang, C. A. Burns, A. H. Said, C. N. Kodituwakku, Y. V. Shvydko, D. Casa, T. Gog, and P. M. Platzman, Phys. Rev. B **81**, 075104 (2010).
- [37] W. Schülke, *Electron Dynamics by Inelastic X-ray Scattering* (Oxford University Press, New York, 2007).
- [38] I. Loa, K. Syassen, G. Monaco, G. Vankó, M. Krisch, and M. Hanfland, Phys. Rev. Lett. **107**, 086402 (2011).
- [39] H.-K. Mao, Y. Ding, Y. Xiao, P. Chow, J. Shu, S. Lebègue, A. Lazicki, and R. Ahuja, Proc. Natl. Acad. Sci. USA **108**, 20434 (2011).
- [40] W. Schülke, U. Berg, and O. Brümmer, Phys. Status Solidi B **35**, 227 (1969).
- [41] G. Priftis, Phys. Rev. B **2**, 54 (1970).
- [42] D. M. Miliotis, Phys. Rev. B **3**, 701 (1971).
- [43] P. Eisenberger, P. M. Platzman, and K. C. Pandey, Phys. Rev. Lett. **31**, 311 (1973).
- [44] S. Huotari, C. Sternemann, M. C. Tropicovsky, A. G. Eguluz, M. Volmer, H. Sternemann, H. Muller, G. Monaco, and W. Schülke, Phys. Rev. B **80**, 155107 (2009).
- [45] S. Huotari, J. A. Soininen, G. Vankó, G. Monaco, and V. Olevano, Phys. Rev. B **82**, 064514 (2010).

- [46] H.-C. Weissker, J. Serrano, S. Huotari, E. Luppi, M. Cazzaniga, F. Bruneval, F. Sottile, G. Monaco, V. Olevano, and L. Reining, *Phys. Rev. B* **81**, 085104 (2010).
- [47] K. Tamura, M. Inui, S. Hosokawa, *Rev. Sci. Instrum.* **70**, 144 (1999).
- [48] K. Matsuda, Ph. D. Thesis, Kyoto University, 2006.
- [49] Y. Q. Cai, P. C. Chow, O. D. Restrepo, Y. Takano, K. Tagano, H. Kito, H. Ishii, C. C. Chen, K. S. Liang, C. T. Chen, S. Tsuda, S. Shin, C. C. Kao, W. Ku, A. G. Eguiluz, *Phys. Rev. Lett.* **97**, 176402 (2006).
- [50] C. H. Macgillavry, G. D. Rieck, *International Tables For X-Ray Crystallography*, Volume III (The Kynoch Press, Birmingham, 1962).
- [51] K. Kimura, K. Matsuda, and M. Yao, *J. Phys. Soc. Jpn.* **82**, 115001 (2013).
- [52] G. D. Mahan, *Many-Particle Physics* (Kluwer Academic/Plenum Press, New York, 2000) 3rd ed., Chap. 9.
- [53] K. Sturm, *Z. Phys. B* **25**, 247 (1976).
- [54] N. W. Ashcroft, *Phys. Lett.* **23**, 48 (1966).
- [55] N. W. Ashcroft, *J. Phys. C* **2**, 232 (1968).
- [56] W. A. Harrison, *Electronic Structure and the Properties of Solids* (Freeman, San Francisco, 1980) p. 362.
- [57] G. Franz, W. Freyland, W. Glaser, F. Hensel, and E. Schneider, *J. Phys. (Paris), Colloq.* **8**, 194 (1980).
- [58] Y. Waseda, *The Structure of Non-Crystalline Materials* (McGraw-Hill, New York, 1980) p. 253.
- [59] N. W. Ashcroft and N. D. Mermin, *Solid State Physics* (Thomson Learning, Inc., New York, 1976).

- [60] T. E. Faber, *Theory of Liquid Metals* (Cambridge University Press, Cambridge, 1972) p. 326.
- [61] K. Kimura, K. Matsuda, N. Hiraoka, T. Fukumaru, Y. Kajihara, M. Inui, and M. Yao, Phys. Rev. B **89**, 014206 (2014).
- [62] K. Hoshino and W. H. Young: J. Phys. F: Met. Phys. **16**, (1986) 1659.
- [63] P. Vashishta and K. S. Singwi, Phys. Rev. B **6**, 875 (1972).
- [64] A. L. Fetter, J. D. Walecka, *Quantum Theory Of Many-Particle Systems* (Dover Publications, Inc. New York, 2003).
- [65] P. Söderlind M. Ross, J. Phys.: Condens. Matter, **12**, 921 (2000).
- [66] A. A. Mirzoev, A. A. Mirzoev Jr, A. N. Sobolev, B. R. Gelchinski, J. Phys.: Condens. Matter, **20**, 114104 (2008)
- [67] J. E. Mayer and M. G. Mayer, Phys. Rev. **43**, 605 (1933).
- [68] K. Kimura, K. Matsuda, N. Hiraoka, Y. Kajihara, T. Miyatake, Y. Ishiguro, T. Hagiya, M. Inui, and M. Yao, submitted to J. Phys. Soc. Jpn..
- [69] B. B. Alchagirov, and A. G. Mozgovoï, High Temp. **44**, 221 (2006).
- [70] K. Matsuda, and K. Tamura, Rev. Sci. Inst. **75**(3), 709 (2004).
- [71] H. P. Pfeifer, W. Freyland, and F. Hensel, Ber. Bunsenges. Phys. Chem. **83**, 204 (1979).
- [72] R. Fischer, Ph. D. Thesis, Philipp University of Marburg, 1978.
- [73] W.-C. Pilgrim, S. Hosokawa, H. Saggau, H. Sinn, and E. Burkel, J. Non-Cryst. Solids **250 - 252**, 96 (1999).